

Nondestructive observation of internal
-color, -structure and -particle-dispersion-state
based on low-coherence interferometry

Sohichiro Nakamura

For my familiy ..

Ayako

Masataka

Takaaki

Kenichiro

Yukiko

Tsunemitsu

Syoko

■ CONTENTS

I Introduction	1
1. Concerns and Problems about Light Propagation and Observation methods from the Visible to the Ultraviolet Region in the Skin.....	3
2. Measurement method and application example Of full-color tomogram and their task	6
3. Particle Size and Dispersion State in Suspension	7
4. Low-coherence interferometry	9
II Principles of Low-Coherence Interferometry, Full-Color Optical Coherence Tomography and Low-Coherence Dynamic Light scattering	10
1. Low-coherence Interferometry	10
2. Full-Color Optical coherence tomography	13
3. Low-coherence dynamic Light scattering	15
III Development of UV- and visible-light one-shot SD-OCT and <i>in-situ</i> measurements of human skin.....	19
1. Method	19
2. Result	21
3. Conclusion	30
IV Development of full-color OCT and <i>in situ</i> measurements of human skin	31
1. Method	31
2. Result	34
3. Conclusion	37
V Development of high-sensitivity low-coherence dynamic light scattering and determinations of particle size distribution and diffusion motion modes applied to dense particle suspensions.....	39
1. Method	39
2. Result	41
3. Conclusion	51
VI Particle distribution of concentrated polydisperse suspension through high sensitivity low-coherence dynamic light scattering	52
1. Method	52
2. Result	55

3. Conclusion 58

VII Conclusion 60

VIII References 61

IX Publications 65

X Conference Presntations 67

Appendix 69

Acknowledgement 71

I Introduction

What we see is a "result" of light that is diffusely reflected and absorbed by objects. Various oil paintings are created by applying many layers of opaque or transparent color on canvas which reflect, absorb, and scatter light to convey the impressions devised by the artist. Textures of the skin vary with the season, the environment, and age. These textures are the results of multiple reflections as well as absorption of light due to the shape of the surface of the skin, the state of the skin cells, and dyes such as melanin and hemoglobin at any given moment. The light propagation and structure inside objects—which become the "cause" of expression and texture—must to be clarified while maintaining the original shape of such valuable objects and substances as precious oil paintings, human skin, and so on.

Direct observation of the color and structure inside the living body and inside the object while maintaining the original state is hoped for in the fields of science, medical care, industry, agriculture, psychology and culture. Such a nondestructive observation technique is required for quality control of industrial products such as skin diagnosis, painting of automobiles and thin display, examination of plants and foods, and research on the texture of cultural properties and crafts (Fig.1). Such non-invasive methods can also be used to observe time changes and dynamic processes.

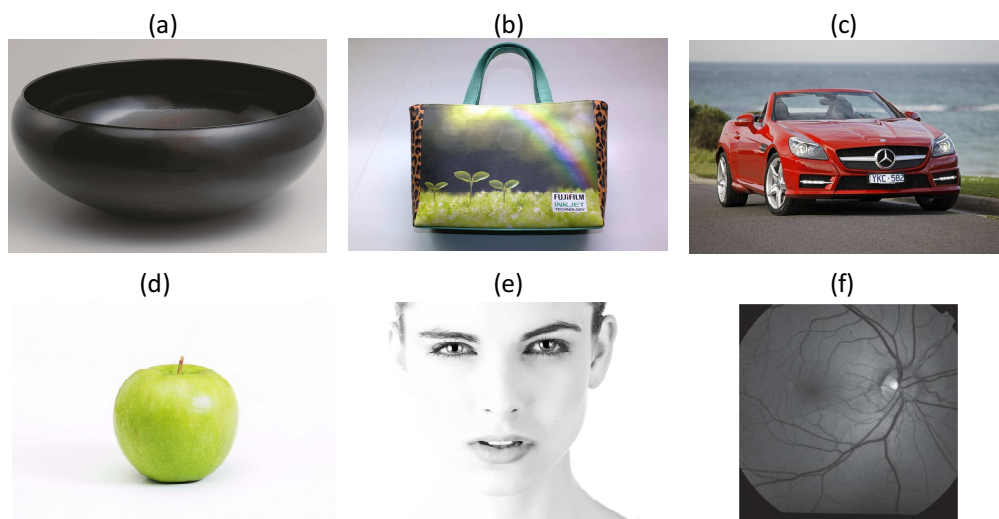


Fig. 1 Nondestructively measuring the color and structure inside the object and the dispersion distribution of the particles such as pigments is required in a wide range of fields, (a) Japanese lacquerware, (b) an inkjet printing bug, (c) a coated product (car), (d) an apple, (e) cosmetic inspection, (f) funduscopy.

Research on the relationship between the skin structure and its sensual texture, which is the basis of how any skin appears, has been conducted in the field of dermatology, color psychology, and computational optics such as computer graphic simulation. Such research has been applied to fundamental studies on cosmetic development and a associated diagnostic technique. The influence of skin color and spatial frequency on appearance as well as the relation between the illumination method and appearance have been actively discussed in psychology. The focus of these studies is spectral reflectance characteristics of the skin. As a subcommittee of the Japanese Color Science Association, "Cosmetics and Skin and Face Study Group" was launched in 2014. Moreover, research promotion movements toward industry-academic science-based skin appearance are being actively undertaken [1]. However, the relationship between the internal structure of the skin and the application state of the cosmetic product and how it looks is not a quantitative consideration, because it is speculative in nature; also, a complex structure inside the skin (Fig. 2).

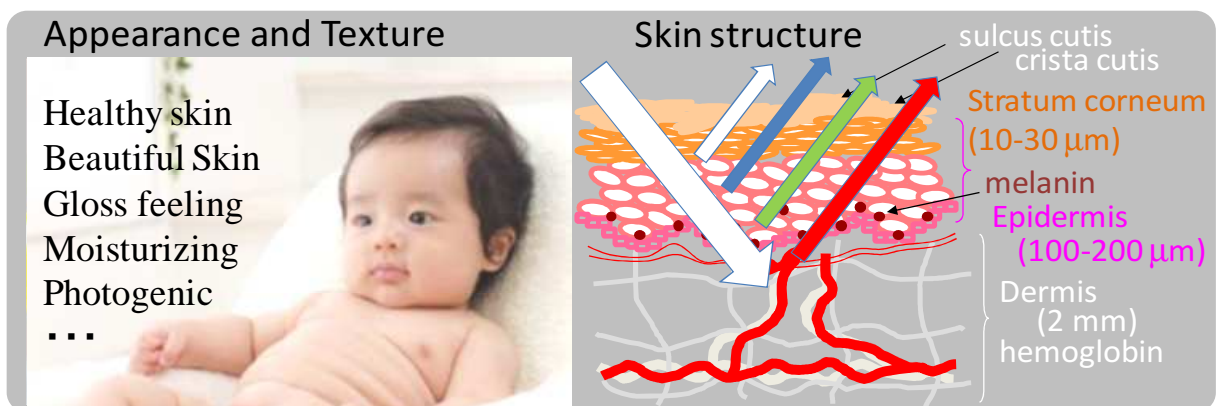


Fig. 2 The appearance and sensitivity of the skin, the internal structure of the skin

There is a need not only for solids but also liquids, such as paints or ink pigments which express colors, inorganic particles which are precursors to nanocomposite materials, and DDS (drug delivery system) which often contain nanoparticles. Such dispersed state of nanoparticles in liquid dominates physical properties such as viscoelasticity and surface tension and its stability is related to storage life of commercial products, such as ink (Fig.3). Thus measurements have to be carried out directly but nondestructively. For example, inks contain largely varying quantities of pigment nanoparticles and also include dispersants, binder polymers, and additives. In such a concentrated dispersed particle system, formation of aggregates by collision and bridging structure between particles through binder polymers is likely to occur; these aggregates make it difficult to develop stable liquid and optical

properties. Quantifying the dispersion structure of the suspension nondestructively will lead to the development of nanoparticle-containing products.

Therefore, it is thought that from light, the "result" of multiple reflections and other optical phenomena, the techniques for clarifying the internal color and structure and light propagation—as "cause"—are required.

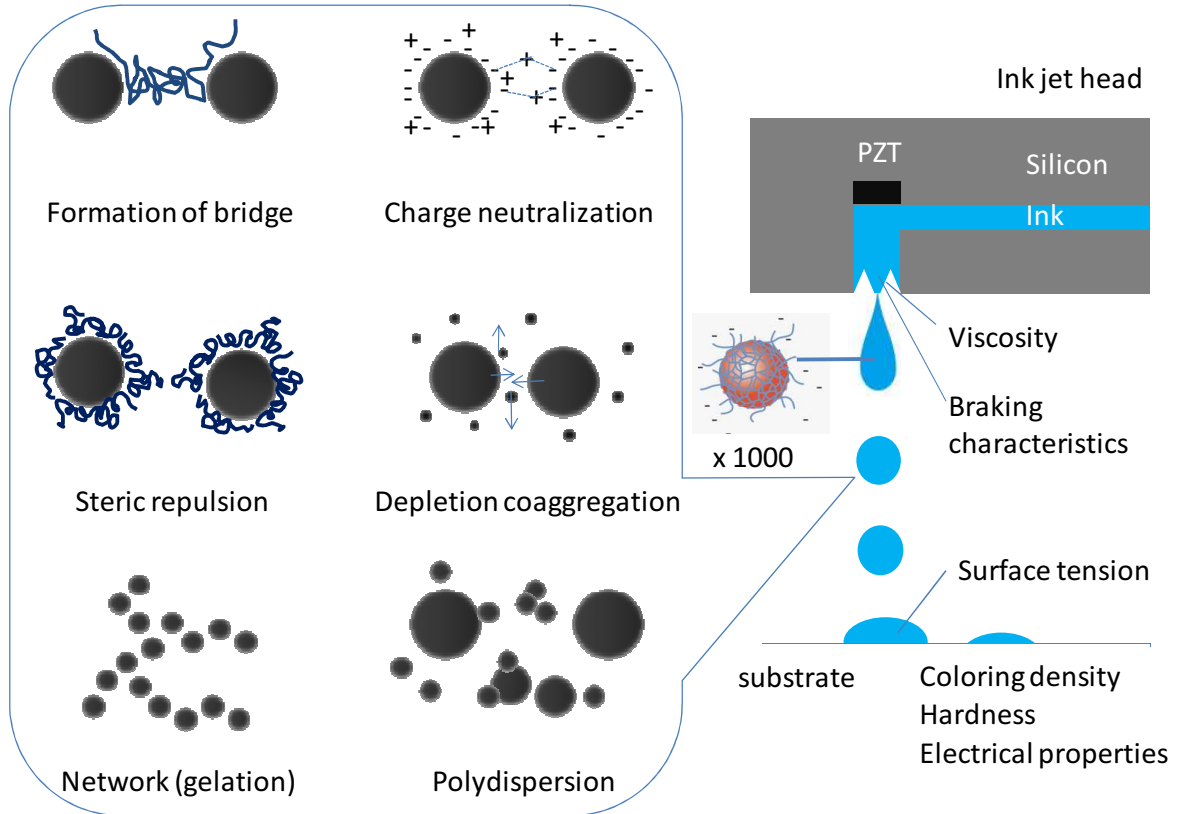


Fig. 3 An example for dispersion state of particles in inkjet that dominates physical properties and product performance.

1. Concerns and Problems about Light Propagation and Observation methods from the Visible to the Ultraviolet Region in the Skin

Human skin changes from season to season and varies depending on the age of an individual and the environment they live in. The appearance and texture of human skin are caused by its surface roughness, inner structure, and the spatial distribution of pigment cells at a given moment. The outermost skin has textures called the sulcus cutis and the crista cutis. These textures are influenced by skin drying conditions, age, and other such factors [2]. Skin consists of the stratum corneum, the epidermis, and the dermis. The thicknesses of these sections are 10–30 μm at the stratum corneum, 100–200 μm at the epidermis, and 2–3 mm at

the dermis (Fig. 2). There are two major pigments in human skin: melanin, which is located in the epidermis, and hemoglobin, which is located in the capillaries in the dermis. Cells are always exposed to numerous risks, such as physical stress, drying, ultraviolet illumination, and free radicals. In addition, several risks to and changes in skin appearance have been reported as a result of UV exposure [3-6]. Cells are created by cell division at the stratum basale, which is attached to the noncellular basement membrane that forms the boundary between the epidermis and the dermis. The new cells are pushed up to the surface in two weeks. Subsequently, those cells begin keratinization and finally peel off over the following two weeks. This process is called *skin turnover*, which is also known as the life cycle of the skin. A study that clarifies the relationship between the appearance and the inner structure of human skin at a given moment is needed for cosmetic industries, dermatology, cosmetics, and numerical simulation [7].

Conventionally, in order to investigate the state of the inside of the skin as well as in the development of medicines such as dermatologists' and percutaneously absorbable preparations where the sizes, shapes and colors of abnormal sites are checked by visual observation or palpation, further detailed analysis is necessary. In such cases, we have performed medical procedures such as cutting out the skin, taking a small amount and then acquiring an image of the pathological section with a microscope. In order to quantify the depth of light reaching the skin, there is an example of measuring the transmittance by changing the thickness of the removed skin [8]. If we can extract information from the inside of the skin concerning color and structure without damaging the skin, characteristics such as change in skin texture and a person's unique skin variances by season and skincare can be clarified *in situ*.

Moreover, it is important to clarify the propagation of ultraviolet (UV) light, which is recognized as the cause of skin damage. However, it is difficult to evaluate human skin without injuring it. A nondestructive measurement is needed to measure the distinctions between each person and the effects of the application of cosmetic or pharmaceutical products.

There is some technique for imaging the tomogram of a living body in the field of the medical test. The tomogram imaging method of the skin structure is already being used in a somascope, a confocal microscope and Optical Coherence Tomography (OCT) (Fig.4). The somascope is commonly used in hospitals and is used to measure depths of more than a millimeter. However, its resolution is 100 μm ; thus it is not suitable for the observation of skin with a keratin structure that is 10–30 μm in thickness. Confocal microscopy cannot be

used to evaluate skin with cosmetics because it covers the skin with match oil; nonetheless, it offers sufficient resolution and measurement depth capability to observe keratinous cells. On the other hand, OCT [9] has been developed as the tomogram imaging method for examinations of the fundus using infrared light of wavelengths having high transmissivity and is called "the window of the living body". Subsequent developments have also been remarkable. Functional OCTs, such as polarization-sensitive OCT [10] and Doppler OCT [11] which can be used to observe collagen fibers in the skin using polarized light and measure blood flow, respectively have been developed. Studies have also been carried out to achieve a high resolution of 1 μm in OCT by using a white light source to shorten the center wavelength and broaden the spectrum width [12].

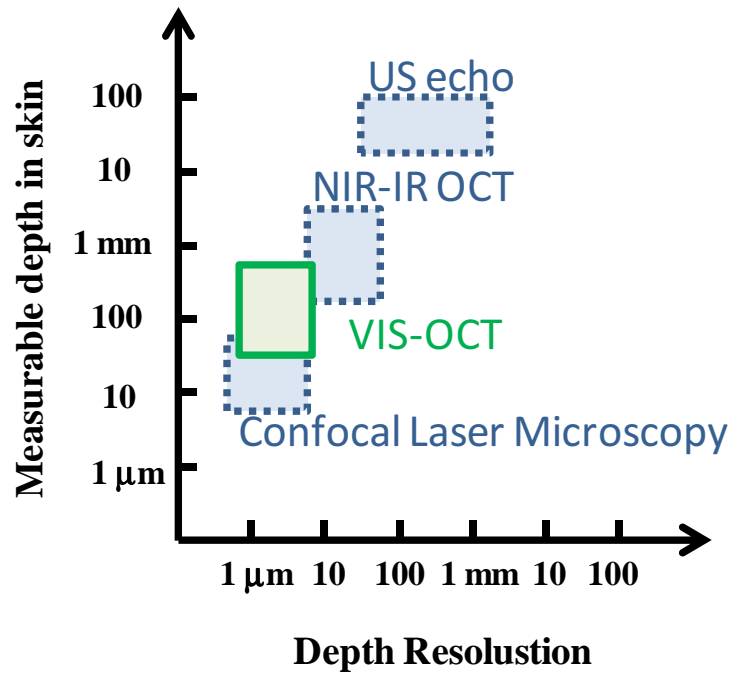


Fig. 4 Measurement depth and high resolution of various tomographic imaging methods for skin observation

In recent years, OCT based on visible light has been reported. Full-field (FF) OCT based on red (R), green (G), and blue (B) light-emitting diode (LED) light sources has been reported; this tomography is used to measure the application thickness of cosmetic foundation and the change in the reflection of each color caused by the application of foundation. It is necessary to operate a sample stage for measurement by FF-OCT; thus, a skin replica has been substituted. In other reports, *in-vivo* human skin non-color images were obtained by FF-OCT with a high resolution (approximately 1 μm) [13]. It is necessary to maintain the same measurement point in human skin with a cover glass during the

measurement. With the application of a moisturizer, the refractive-index matching between the stratum corneum and the cover glass changes and thus the imaging depth of tomography increases. Consequently, it is difficult to evaluate the skin with cosmetics in its natural state because of the cover glass. Only red–NIR light has been used for measurement, and images with B and G light have not been obtained. The measurement of a human finger by Spectral Domain (SD) OCT using a superluminescent diode (SLD) with a wavelength of 680 nm, 840 nm, or 930 nm has been reported [14]. In another report, a broadband visible–NIR light source was used without spectroscopic dispersion to achieve a high depth resolution [15]. Therefore, there are no reports on visible-light OCT for the systematic evaluation of a tomogram of human skin with RGB light because too much to measure depth of observation for medical use and the wavelength range of the light source. In addition, there are no reports on OCT of human skin within the UV-light region

2. Measurement method and application example of full-color tomogram and their task

As described in the previous section, if a tomographic image at a wavelength in the visible range can be obtained, information on the true color inside the living body and the object can be acquired. Recently, the color tomogram images of a mouse dorsal skinfold window chamber model were studied by a type of SD-OCT called true-color OCT. This method utilized a 450–700 nm wavelength region and calculated the spectrum arithmetically using the dual window processing method [16–18]. A visible SD-OCT with a 496–632 nm wavelength region was applied to carry out a mouse angiography [19]. However, owing to the presence of melanin or hemoglobin pigment, there is no report on studying color information inside the skin (human skin) with strong light absorption.

For full colorization, I must develop a way to simultaneously measure more than three colors. Moreover, to visualize color information inside the skin, it is necessary to reproduce the color of the lower layer which is under the influence of scattering from the upper layer and the absorption layer. The melanin pigment's absorption of light and its scattering by cells in the epidermis affect the apparent color of human skin. Fig. 5 is a conceptual diagram for considering the influence in the case where the upper layer is red as an example. A two-layer model structure that consists of red at top layer and white at bottom layer is shown in the figure. In OCT measurements, the apparent color of scattered lights from the lower layer is the result of absorption in the upper layer. These absorption layers also affect the decoherence of light and the degradation in image quality for a wide-band or a white band SD-OCT light source.

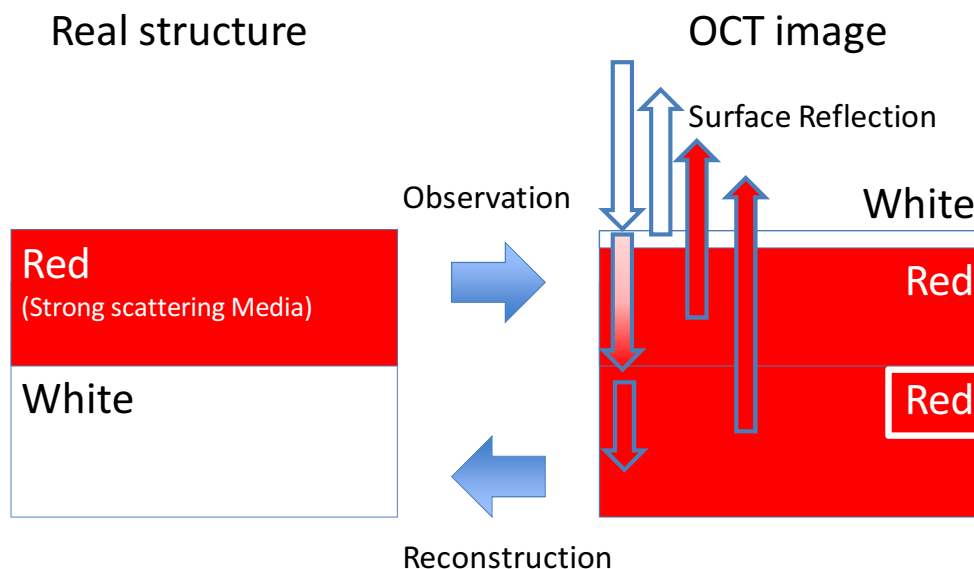


Fig. 5 The relation between the real color of the lower layer and OCT layer color.

3. Particle Size and Dispersion State in Suspension

Nanoparticles are widely used as organic pigments in paints and inks or as inorganic precursors of nanocomposites and functional materials [20-23]. In a colloidal suspension, aggregates of particles deteriorate aging stability and performance over time and their dispersed state dominates the physical properties such as viscoelasticity and surface tension. For example, consider an ink consisting of 1–30% pigment nanoparticles, a dispersant, binder polymers, and additives. In such a dense suspension, aggregates are likely to form by collisions between particles or bridging flocculations via the binder polymer; such aggregates deteriorate the physical and optical stability of the suspensions (Fig. 3).

Dynamic light scattering (DLS) [24] can quantify the sizes of particles in a solution with nanoparticles and macromolecules and is commonly used to inspect such solutions. To accurately detect the fluctuation of the scattered light undergoing Brownian motion, DLS usually proceeds after the particle concentration in the dispersion has been adjusted to 0.1 to 0.001 wt% for eliminating multiplescattering (Fig. 6). However, the particle-size distribution in this diluted state may differ from the actual dispersity of the suspension.

Since the latter half of the 1990's, the fluctuation of scattered light and the anisotropic parameter g , both of which depend on the optical path length in a medium that strongly scatters light, have been studied quantitatively using time-resolved spectroscopy or low-coherence interferometers [25-27]. The combination of these methods is called

low-coherence DLS (LC-DLS); LC-DLS method can extract single scattering events. Polystyrene particles in dense suspensions have been quantitatively analyzed with this method [28-31]. In recent years, LC-DLS systems, with fine optical path length resolution, that use supercontinuum and spectral-domain interferometers have been developed and have found application in measurements at solid-liquid interfaces [32-33]. Although LC-DLS is an effective method for measuring the dispersity of a dense suspension non-destructively, these systems have not been tested quantitatively with particles smaller than 100 nm. Generally, nanoparticles have diameters between several nanometers and several tens of nanometers, and nanoparticle aggregates in a polydisperse state have diameters ranging from tens to several hundreds of nanometers. Therefore, the scale of particle sizes that need to be measured spans five orders of magnitude. No reports have been published so far about quantitative analysis of such a polydisperse state in a concentrated system.

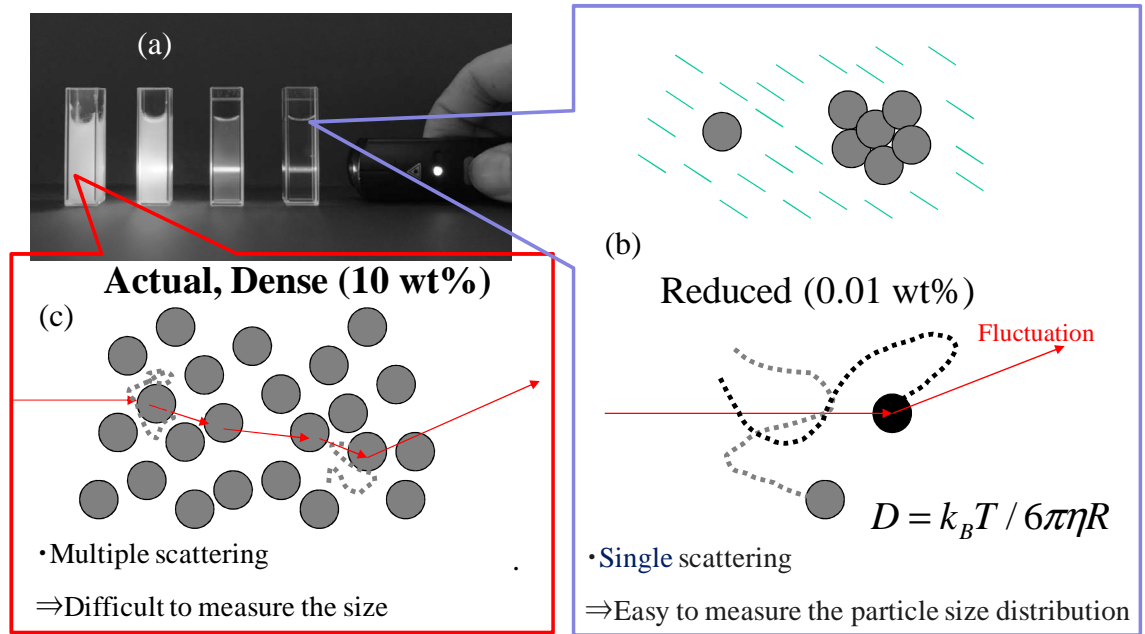


Fig. 6 Optical scattering and particle sizing (a) A photograph of a polystyrene dispersion solution having a higher dilution ratio as it goes from left to right was irradiated with a laser pointer, (b) Single scattering occurred in dilute solution, (c) Multiple Scattering occurred in actual, dense suspension.

In addition, the entire dispersion system may behave like a gel because of a dispersant or a polymer existing between the particles; also, it is necessary to specify the motion mode, that is, whether it is floating and performing the Brownian motion. Development to address

the requirements of industry has not been sufficient.

4. Low-coherence interferometry

Low-coherence interferometry (LCI) is a noncontact and nondestructive depth profile measurement technique by using the coherency of the light. A low coherent light is in an intermediate state between of absolute coherent limit and incoherent limit. In other word, a low coherent light means a partial coherent light. Representative example of coherent light source is a LASER (Light Amplification by Stimulated Emission of Radiation) of which the wavelength and the phase are unity. The examples of low coherent light sources are a LED (Light Emitted Diode), a SLD (Superluminescent Diode), a SC (Supercontinuum) Light source and a Xenon lamp that wavelengths and phases are not unity and partially disorderd. By adjusting a LCI's optical path length that interference occurs, the reflected or transmitted light signal of a sample in the depth region of the aim is acquired.

In this report, I presented developments of measurement systems of inner-color, -structure, and -particle dispersion state inside a living body, a solid and a liquid, based on low-coherence interferometry to extract information of an aiming position of a sample which caused multiple scattering and reflection of a light. In addition, I also showed interpretation and consideration of the observations.

II Principles of Low-Coherence Interferometry, Full-Color Optical Coherence Tomography and Low-Coherence Dynamic Light Scattering

Scattering

1. Low-coherence interferometry

Low-coherence interferometers are classified into two types, one is a time domain (TD) interferometer and the other is a spectral domain (SD) interferometer. In this paper, I used the TD interferometer for the low-coherence dynamic light scattering (LC-DLS) system and the SD interferometer for the OCT systems.

1) Time Domain Interferometry

A basic setup of TD interferometry is shown in Fig. 7. A low coherent source emits a light beam and the beam is passing through inside the fiber to the photo coupler. The light is divided to two beams by the photo coupler, one is propagate to the reference arm line and the other is sample arm line. Reference beam is reflected by the mirror and recollected into the fiber by a collimation lens. Sample beam is irradiated into the sample and the scattered lights inside the sample are collected by a collimation lens into the fiber. Then Scattered lights and reference light beam are interfere and detected by the photo detector.

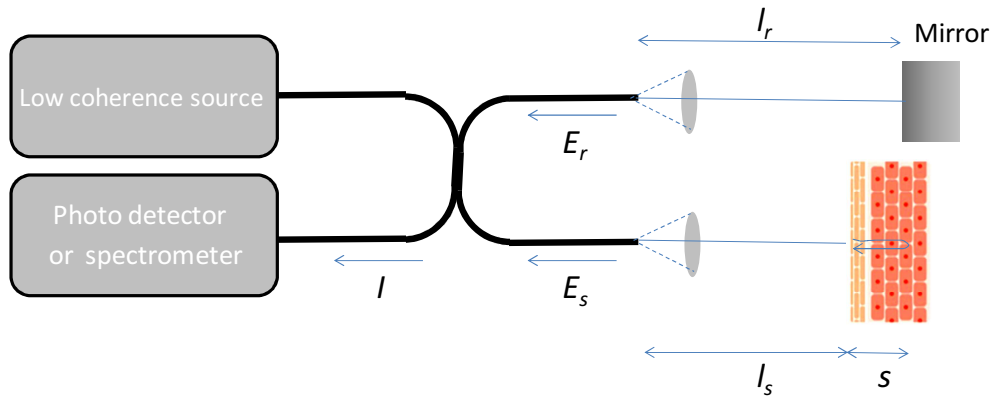


Fig. 7 A basic setup for Low coherent interferometry. TD interferometry detects the light intensity by photodetector and SD interferometry detects the spectrum by spectral photometer.

In TD, the intensity $I(t)$ detected are given by

$$\begin{aligned} I(t) &= |E_s(t) + E_r(t)|^2 \\ &= |E_s(t)|^2 + |E_r(t)|^2 + E_s(t)E_r^*(t) + E_s^*(t)E_r(t) , \end{aligned} \quad (1)$$

where $*$ denotes a complex conjugate, $E_s(t)$ is the electric amplitude from the sample at time t and $E_r(t)$ is the amplitude from the reference. The electric field of a sample at the detector is expressed as

$$E_s = \int_{-\infty}^{\infty} E_0 \left(t - \frac{2l_s + 2s}{c} \right) \cdot R_s(s) \cdot e^{i\{2k(l_s + s) - \omega t\}} ds , \quad (2)$$

where E_0 is the electric field of the light source and $R(s)$ is the reflection rate of the sample at an optical depth s . In Eq. (2), l_s , c , k , and ω are the optical path length between the edge of the air/fiber interface and the sample surface as Fig. 7, the light speed, the wavenumber and the angular frequency of the light, respectively. In Eq. (2), the common paths of the reference beam and the sample beam are omitted. The electric field of reference is expressed as

$$E_r = R_m E_0 \left(t - \frac{2l_r}{c} \right) \cdot e^{i(2kl_r - \omega t)} , \quad (3)$$

where E_0 is the electric field of the light source and R_m is the reflection rate of the mirror. l_r is the optical path length between the fiber and the mirror surface.

The first, second and third term of Eq. (1) are rewritten using Eqs. (2) and (3) as

$$|E_s(t)|^2 = \int_{-\infty}^{\infty} \int_{-\infty}^{\infty} R_s(s) R_s^*(s') \cdot E_0 \left(t - \frac{2l_s + 2s}{c} \right) E_0^* \left(t - \frac{2l_s + 2s'}{c} \right) \cdot e^{i2k(s' - s)} ds ds' \quad (4)$$

$$= \int_{-\infty}^{\infty} \int_{-\infty}^{\infty} R_s(s) R_s^*(s + \Delta s) \cdot E_0(t) E_0^* \left(t - \frac{2\Delta s}{c} \right) \cdot e^{i2k\Delta s} ds d(\Delta s),$$

$$|E_r(t)|^2 = R_m^2 E_0^2 \left(t - \frac{2l_s + 2s}{c} \right), \quad (5)$$

$$\begin{aligned} E_s(t) E_r^*(t) &= \int_{-\infty}^{\infty} E_0 \left(t - \frac{2l_s + 2s}{c} \right) E_0^* \left(t - \frac{2l_r}{c} \right) \cdot R_m R_s(s) \cdot e^{i2k(l_s - l_r + s)} ds \\ &= \int_{-\infty}^{\infty} E_0(t) E_0^*(t + \tau) \cdot R_m R_s(s) \cdot e^{i\omega\tau} ds, \end{aligned} \quad (6)$$

where Δs is defined as $\Delta s = s' - s$. In Eq (6), τ is defined as

$$c\tau \equiv 2(l_s - l_r + s). \quad (7)$$

A coherence function of a light source Γ_0 is defined as

$$\Gamma_0(\tau) \equiv \int_{-\infty}^{\infty} E_0(t) E_0^*(t + \tau) dt, \quad (8)$$

and the autocorrelation function of the reflection profile inside the sample is defined as

$$\Gamma_s(\Delta s) \equiv \int_{-\infty}^{\infty} R_s(s) R_s(s + \Delta s) ds. \quad (9)$$

The time average of Eqs. (4)-(6) are

$$\begin{aligned} \langle |E_s(t)|^2 \rangle &= \lim_{T \rightarrow 0} \frac{1}{T} \int_0^T |E_s(t)|^2 dt \\ &= \lim_{T \rightarrow 0} \frac{1}{T} \int_0^T \int_{-\infty}^{\infty} \int_{-\infty}^{\infty} R_s(s) R_s^*(s + \Delta s) \cdot E_0(t) E_0^*\left(t - \frac{2\Delta s}{c}\right) \cdot e^{i2k\Delta s} ds d(\Delta s) dt \\ &= \int_{-\infty}^{\infty} \Gamma_s(\Delta s) \cdot \Gamma_0\left(\frac{2\Delta s}{c}\right) \cdot e^{i2k\Delta s} d(\Delta s) \\ &\xrightarrow{\Gamma_0 \approx \delta(\Delta s)} \Gamma_s(0), \end{aligned} \quad (10)$$

$$\begin{aligned} \langle |E_r(t)|^2 \rangle &= \lim_{T \rightarrow 0} \frac{1}{T} \int_0^T |E_r(t)|^2 dt \\ &= R_m^2 \cdot \lim_{T \rightarrow 0} \frac{1}{T} \int_0^T |E_0(t)|^2 dt \\ &= R_m^2 I_0, \end{aligned} \quad (11)$$

$$\begin{aligned} \langle E_s(t) E_r^*(t) \rangle &= \lim_{T \rightarrow 0} \frac{1}{T} \int_0^T E_s(t) E_r^*(t) dt \\ &= \lim_{T \rightarrow 0} \frac{1}{T} \int_0^T \int_{-\infty}^{\infty} E_0(t) E_0^*(t + \tau) \cdot R_m R_s(s) \cdot e^{i\omega\tau} ds dt \\ &= \int_0^{\infty} \Gamma_0(\tau) \cdot R_m R_s(s) \cdot e^{i\omega\tau} ds \\ &= \int_0^{\infty} \Gamma_0\left(\frac{2(l_s - l_r + s)}{c}\right) \cdot R_m R_s(s) \cdot e^{i\omega \frac{2(l_s - l_r + s)}{c}} ds \\ &\xrightarrow{\Gamma_0 = \delta\left(\frac{l_s - l_r + s}{c}\right)} R_m R_s(l_r - l_s). \end{aligned} \quad (12)$$

In Eqs (10)-(12), the relation $\Gamma_0 = \delta(t)$ is used because an ideal low coherence light source indicates the Γ_0 term close to delta function.

Simply, Eqs. (1) and (10)-(12) yield the time average light intensity detected

$$\langle I \rangle = R_m^2 I_0 + \Gamma_s(0) + 2R_m R_s(l_r - l_s). \quad (13)$$

In Eq. (13), as the first and the second term are constants, thus the depth profile is obtained by moving the reference optical path length l_r . More precise calculation applies to Eq. (13) is that the coherence of the light source is convoluted, note that neglect the term in

calculation of (10)-(12).

2) Spectral Domain Interferometry

An example setup of SD interferometry is almost same as TD as shown in Fig. 7. The light spectrum detected by spectrometer is

$$\begin{aligned} I(k) &= |E_s(k) + E_r(k)|^2 \\ &= |E_s(k)|^2 + |E_r(k)|^2 + E_s(k)E_r^*(k) + E_s^*(k)E_r(k) \end{aligned} \quad (14)$$

A scattering light amplitude spectrum from the sample is described as:

$$E_s(k) = \int_0^\infty E_s(z) \cdot e^{i2kz} dz, \quad (15)$$

where z indicates a depth from the sample surface.

Performing an inverse Fourier transform to Eq. (14) and by using (15), the following is obtained

$$\begin{aligned} I(z) &= F^{-1}(I(k)) \\ &= \Gamma_{E_s}(z) + \Gamma_{E_r}(z) + \Gamma_{E_s E_r}(z) + \Gamma_{E_s E_r}^*(z) \\ &= I_r \delta(z) + 2\sqrt{I_r} \cdot \text{Re}(E_s(z)) + \Gamma_{E_s}(z) \end{aligned} \quad (16)$$

In Eq. (16), convolution of coherence of optical light source is omitted. The first term of Eq. (16) shows the signal around $z=0$, the second term corresponds to the sample depth profile, the third term is autocorrelation of the sample electric field that is weaker than the second term. Thus the depth profile is obtained by inverse Fourier transformation of a spectrum of a SD low-coherence interferometry.

2. Full-Color Optical Coherence Tomography (OCT)

OCT is a scattering medium imaging method based on a low-coherence interferometry. By using a scan light beam of a galvanometer mirror or an imaging camera with a low-coherence interferometer, 2D and 3D tomogram imaging can be obtained.

1) Color reproduction for a full-color OCT

In CIE (Commission Internationale de l'Éclairage) XYZ color space, X , Y , and Z tri-stimulus values of a spectrum $P(\lambda)$ are expressed as:

$$X = \alpha_x \cdot \int P(\lambda) \bar{x}(\lambda) d\lambda \quad (17)$$

$$Y = \alpha_Y \cdot \int P(\lambda) \bar{y}(\lambda) d\lambda \quad (18)$$

$$Z = \alpha_Z \cdot \int P(\lambda) \bar{z}(\lambda) d\lambda \quad (19)$$

In eqs (17)-(19), \bar{x} , \bar{y} , \bar{z} are color matching functions and α_X , α_Y , α_Z are device sensitivity factors for R , G , and B colors, respectively. XYZ tri-stimulus values changed to RGB values by:

$$\begin{pmatrix} R \\ G \\ B \end{pmatrix} = \begin{pmatrix} 2.365 & -0.897 & -0.468 \\ -0.515 & 1.426 & 0.089 \\ 0.005 & -0.014 & 1.009 \end{pmatrix} \begin{pmatrix} X \\ Y \\ Z \end{pmatrix} \quad (20)$$

A whole color image of a full-color OCT is constructed by R, G, B OCT intensity images. A value of a pixel of each color image is converted to 256 tones. Each pixel of every R, G, B image are combined and then a color image are built. Device sensitivity factor α_X , α_Y , and α_Z are determined by using a standard sample such as white as in Fig. 23, experimentally. When an OCT signal is affected by the speckle or signal-to-noise ratio is not enough for a real-time imaging, it is effective to special filtering using surrounding pixels.

2) Light attenuation in a strong scattering medium

A light intensity inside an object in the depth z is expressed as:

$$I(z) = I_0 e^{-(\mu_s + \mu_a)z} \quad (21)$$

where μ'_s and μ_a indicate a reduced scattering coefficient and an absorption coefficient respectively. A reduced scattering coefficient is expressed as

$$\mu'_s = (1 - g)\mu_s \quad (22)$$

where μ_s indicate a scattering coefficient of the object. In Eq. (22), g is the anisotropy factor. For a forward scattering media like skin, a g values is known as 0.75 – 0.95 [34]. An anisotropy g is expressed with phase function $p(\theta)$ which implies the scattering angle distribution:

$$g = \int_0^\pi p(\theta) \cos \theta 2\pi \sin \theta d\theta \quad (23)$$

For a strong scattering media such as a biological tissue, $p(\theta)$ is expressed as Henyee-Greenstein function:

$$p(\theta) = \frac{1}{4\pi} \cdot \frac{1 - g^2}{(1 + g^2 - 2g \cos \theta)^{3/2}} \quad (24)$$

Note that Eq. (16) shows the SD-OCT signal intensity is corresponded to a electric field E and Eq (21) shows the intensity. So the electric field is :

$$E_s = \sqrt{I_s} = E_0 e^{-\frac{1}{2}(\mu_s + \mu_a)z} = E_0 e^{-\frac{1}{2}\mu z} \quad (25)$$

The signal intensity of the depth z is reduced $\exp(-\mu z)$ times because the sum of optical pathlength of incident light and scattering lights is $2z$. Therefore the OCT signals at depth z are able to be compensated by multiplying the signal intensity by $\exp(\mu z)$. In general, OCT-signal sensitivity is not a constant for z -direction to be affected by an object lens condensing efficiency difference of back-scattering lights and a point spread function, thus it is necessary to compensate the influence by a measurement of reflection intensity by a standard mirror sample by moving in z -direction.

3. Low-coherence dyanamic light scattering (LC-DLS)

A LC-DLS system based on a TD interferometry is shown in Fig. 7. The power $P_I(t)$ is detected by a photometer is inverse Fourier transform of $P_I(\omega)$,

$$P_I(t) = \frac{1}{2\pi} \int_{-\infty}^{\infty} P_I(\omega) e^{i\omega t} d\omega, \quad (26)$$

and also $P_I(\omega)$ can expressed by $I(\omega)$:

$$\begin{aligned} P_I(\omega) &= I(\omega) \cdot I^*(\omega) \\ &= \int_{-\infty}^{\infty} \int_{-\infty}^{\infty} I(t) I^*(t') e^{-i\omega(t-t')} dt dt' \\ &= \int_{-\infty}^{\infty} \Gamma_I(\tau) e^{-i\omega\tau} d\tau, \end{aligned} \quad (27)$$

where $\Gamma_I(\tau)$ is a temporal autocorrelation function of the detector singnal. Furthermore $P_I(\omega)$ can expressed by electric field E :

$$\begin{aligned} P_I(\omega) &= I(\omega) \cdot I^*(\omega) \\ &= \int_{-\infty}^{\infty} \int_{-\infty}^{\infty} I(t) I^*(t') e^{-i\omega(t-t')} dt dt' \\ &= \int_{-\infty}^{\infty} \int_{-\infty}^{\infty} \{E_s(t) + E_r(t)\} \{E_s^*(t) + E_r^*(t)\} \{E_s(t') + E_r(t')\} e^{-i\omega(t-t')} dt dt', \end{aligned} \quad (28)$$

Eq. (28) is expanded into 16 terms:

$$\begin{aligned} P_I(\omega) &= \int \left\{ \langle E_s(t) E_s^*(t) E_s^*(t') E_s(t') \rangle + \langle E_s(t) E_s^*(t) E_s^*(t') E_r(t') \rangle + \langle E_s(t) E_s^*(t) E_r^*(t') E_s(t') \rangle + \langle E_s(t) E_s^*(t) E_r^*(t') E_r(t') \rangle \right. \\ &\quad + \langle E_s(t) E_r^*(t) E_s^*(t') E_s(t') \rangle + \langle E_s(t) E_r^*(t) E_s^*(t') E_r(t') \rangle + \langle E_s(t) E_r^*(t) E_r^*(t') E_s(t') \rangle + \langle E_s(t) E_r^*(t) E_r^*(t') E_r(t') \rangle \\ &\quad \left. + \langle E_r(t) E_s^*(t) E_s^*(t') E_s(t') \rangle + \langle E_r(t) E_s^*(t) E_s^*(t') E_r(t') \rangle + \langle E_r(t) E_s^*(t) E_r^*(t') E_s(t') \rangle + \langle E_r(t) E_s^*(t) E_r^*(t') E_r(t') \rangle \right\} \end{aligned}$$

$$\begin{aligned}
& + \langle E_r(t)E_r^*(t)E_s^*(t')E_s(t') \rangle + \langle E_r(t)E_r^*(t)E_s^*(t')E_r(t') \rangle + \langle E_r(t)E_r^*(t)E_r^*(t')E_s(t') \rangle + \langle E_r(t)E_r^*(t)E_r^*(t')E_r(t') \rangle \} \\
& \times e^{-i\omega(t-t')} dt dt' \quad , \quad (29)
\end{aligned}$$

where

$$\langle \dots \rangle \equiv \int \dots dt .$$

In Eq. (29), By using cumulant expansion of Gaussian process [35,36],

$$\langle ABCD \rangle = \langle AB \rangle \langle CD \rangle + \langle AC \rangle \langle BD \rangle + \langle AD \rangle \langle BC \rangle . \quad (30)$$

In Eq. (30) , odd moments ($\langle A \rangle$, $\langle ABC \rangle$) are zero. By setting $t' = t + \tau$, each term in Eq. (29) is expanded as:

$$\begin{aligned}
& \text{term 1} = \langle I_s(t)I_s^*(t') \rangle = \Gamma_{I_s}(\tau) \\
& \text{term 2} = \langle E_s(t)E_s^*(t) \rangle \langle E_s^*(t')E_r(t') \rangle + \langle E_s(t)E_s^*(t') \rangle \langle E_s^*(t)E_r(t') \rangle \\
& \quad = \langle I_s \rangle \Gamma_{E_s E_r}^*(0) + \Gamma_{E_s}(\tau) \Gamma_{E_s E_r}^*(\tau) \\
& \text{term 3} = \langle I_s \rangle \Gamma_{E_s E_r}^*(0) + \Gamma_{E_s}^*(\tau) \Gamma_{E_s E_r}(\tau) \\
& \text{term 4} = \langle I_r(t)I_r^*(t') \rangle = \Gamma_{I_r}(\tau) \\
& \text{term 5} = \langle I_s \rangle \Gamma_{E_s E_r}^*(0) + \Gamma_{E_s}(\tau) \Gamma_{E_r E_s}^*(\tau) \\
& \text{term 6} = \langle E_s(t)E_r^*(t) \rangle \langle E_s^*(t')E_r(t') \rangle + \langle E_s(t)E_s^*(t') \rangle \langle E_r^*(t)E_r(t') \rangle + \langle E_s(t)E_r(t') \rangle \langle E_r^*(t)E_s^*(t') \rangle \\
& \quad = |\Gamma_{E_s E_r}(0)|^2 + \Gamma_{E_s}(\tau) \Gamma_{E_r}(\tau) \\
& \text{term 7} = \langle E_s(t)E_r^*(t) \rangle \langle E_r^*(t')E_s(t') \rangle + \langle E_s(t)E_r^*(t') \rangle \langle E_r^*(t)E_s(t') \rangle = |\Gamma_{E_s E_r}(0)|^2 + |\Gamma_{E_s E_r}(\tau)|^2 \\
& \text{term 8} = \langle I_r \rangle \Gamma_{E_s E_r}^*(0) + \Gamma_{E_r}^*(\tau) \Gamma_{E_r E_s}(\tau) \\
& \text{term 9} = \langle I_s \rangle \Gamma_{E_r E_s}^*(0) + \Gamma_{E_s}^*(\tau) \Gamma_{E_r E_s}(\tau) \\
& \text{term 10} = (\text{term 7})^* \\
& \text{term 11} = (\text{term 6})^* \\
& \text{term 12} = \langle I_r \rangle \Gamma_{E_r E_s}^*(0) + \Gamma_{E_r}(\tau) \Gamma_{E_s E_r}^*(\tau) \\
& \text{term 13} = \langle I_r(t)I_s^*(t') \rangle = \Gamma_{I_r I_s}(\tau) = \Gamma_{I_s I_r}^*(-\tau) \\
& \text{term 14} = \langle I_r \rangle \Gamma_{E_s E_r}^*(0) + \Gamma_{E_r}^*(\tau) \Gamma_{E_r E_s}(\tau) \\
& \text{term 15} = \langle I_r \rangle \Gamma_{E_r E_s}^*(0) + \Gamma_{E_r}^*(\tau) \Gamma_{E_r E_s}(\tau) \\
& \text{term 16} = \langle I_r(t)I_r^*(t') \rangle = \Gamma_{I_r}(\tau)
\end{aligned} \quad (31)$$

where $\langle e^{i\omega t} \rangle = 0$ is used as random fluctuation of light amplitude. In Eq. (31), Γ_X denotes

autocorrelation fuction of a physical parameter X and $\Gamma_{X,Y}$ denotes cross-correlation fuction between X and Y. A $\Gamma_{X,Y}$ term indicate an interference compornet. By using Eqs. (31), Γ_I is expressd as :

$$\begin{aligned}
\Gamma_I &= \{\Gamma_{I_s}(\tau) + \Gamma_{I_r}(\tau) + \Gamma_{I_s I_r}(\tau) + \Gamma_{I_s I_r}(-\tau)\} + 4|\Gamma_{E_s E_r}(0)|^2 \\
&\quad + 2|\Gamma_{E_s E_r}(\tau)|^2 + 2\{\Gamma_{E_s}(\tau)\Gamma_{E_r}(\tau) + \text{c.c.}\} + 2\langle I_s \rangle \{\Gamma_{E_s E_r}(0) + \text{c.c.}\} + 2\langle I_r \rangle \{\Gamma_{E_s E_r}(0) + \text{c.c.}\} \\
&\quad + \{\Gamma_{E_s}(\tau) + \Gamma_{E_r}(\tau)\} \{\Gamma_{E_s E_r}^*(\tau) + \Gamma_{E_r E_s}^*(\tau)\} + \{\Gamma_{E_s}^*(\tau) + \Gamma_{E_r}^*(\tau)\} \{\Gamma_{E_s E_r}(\tau) + \Gamma_{E_r E_s}(\tau)\} \\
&= \{\Gamma_{I_s}(\tau) + \Gamma_{I_r}(\tau) + \Gamma_{I_s I_r}(\tau) + \Gamma_{I_s I_r}(-\tau)\} \\
&\quad + \{\Gamma_{E_s}(\tau) + \Gamma_{E_r}(\tau)\} \{\Gamma_{E_s E_r}^*(\tau) + \Gamma_{E_r E_s}^*(\tau)\} + \text{c.c.} + 2|\Gamma_{E_s E_r}(\tau)|^2 + 2\{\Gamma_{E_s}(\tau)\Gamma_{E_r}(\tau) + \text{c.c.}\} \\
&\quad + 4|\Gamma_{E_s E_r}(0)|^2 + 2\langle I_s \rangle \{\Gamma_{E_s E_r}(0) + \text{c.c.}\} + 2\langle I_r \rangle \{\Gamma_{E_s E_r}(0) + \text{c.c.}\} \quad . \quad (32)
\end{aligned}$$

Since the light sorce is an ideal incoherence light emitted, $\Gamma_{I_r}(\tau)$ and $\Gamma_{E_r}(\tau)$ are regard as delta fuctions, in addition, $\Gamma_{E_r}(\tau) = I_r \Gamma_0(\tau)$. Furthermore $\Gamma_{I_s}(\tau)$ is regard as zero when scattering intensity is sufficiency weak against the reference light intensity. And $\Gamma_{E_s E_r} = 0$. So Eq. (32) is expressed as:

$$\begin{aligned}
\Gamma_I(\tau) &= 2\{\Gamma_{E_s}(\tau)\Gamma_{E_r}(\tau) + \text{c.c.}\} + \text{Const} \\
&= 2I_r \Gamma_0(\tau) \text{Re}[\Gamma_{E_s}(\tau)] + \text{Const} \quad . \quad (33)
\end{aligned}$$

And also Eq. (33) is expressed as, by using Eq. (27):

$$P_I(\omega) = 2I_r p_0(\omega) \otimes \text{Re}[p_{E_s}(\omega)] + C\delta(\omega) \quad . \quad (34)$$

By vibrating the reference mirror, the first term in Eq. (34) can be picked up form the power spectrum. Then by invers Fourier transform the componet changes to time correlation function $\Gamma_{E_s}(\tau)$ of light amplitude from the sample that originated from the Brownian motions in sample suspension. All the procedure of paricle sizing of LC-DLS is shown in Fig.8.

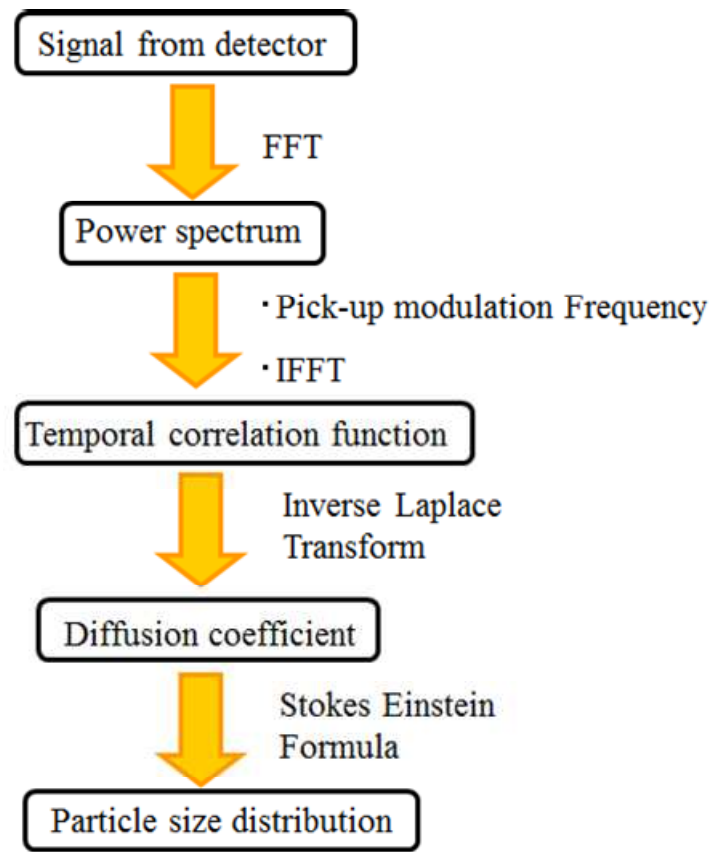


Fig. 8 A Procedure of a particle size measurement of LC-DLS

III Development of UV- and visible-light one-shot SD-OCT and *in-situ* measurements of human skin

I have developed UV- and visible-light one-shot spectral domain (SD) optical coherence tomography (OCT) that enables *in-situ* imaging of human skin with an arbitrary wavelength in the ultraviolet (UV)–visible-light region (370–800 nm). I alleviated the computational burden for each color OCT image by physically dispersing the irradiating light with a color filter. The system consists of SD-OCT with multicylindrical lenses; thus, mechanical scanning of the mirror or stage is unnecessary to obtain an OCT image. Therefore, only a few dozens of milliseconds are necessary to obtain single-image data. I acquired OCT images of one subject's skin *in-vivo* and of a skin excision *ex-vivo* for red (R, 650 ± 20 nm), green (G, 550 ± 20 nm), blue (B, 450 ± 20 nm), and UV (397 ± 5 nm) light. In the visible-light spectrum, R light penetrated the skin and was reflected at a lower depth than G or B light. On the skin excision, I demonstrated that UV light reached the dermal layer. I anticipated that basic knowledge about the spectral properties of human skin in the depth direction could be acquired with this system.

1. Method

1) System

The optical system for UV- and visible-light one-shot SD-OCT is shown in Fig. 9. The light source (an ultrabroadband supercontinuum laser, SC400, Fianium) has a wavelength ranging from 370 nm to 2400 nm, a pulse width of 6 ps, and a repetition rate of 40 MHz. Light is fixed at the central wavelength of any visible level and with wavelength width by a color filter. The source light beam is split into two beams—the sample light beam and reference light beam—by a quartz substrates beam splitter. The sample light beam is linearly focused on human skin by an achromatic cylindrical lens (CL1). We use CL3 behind the quartz substrate for the object lens in the y direction of human skin. I use a beam expander (BE) to improve the resolution in the y direction by increasing the magnification ratio of the image. Light propagates into the spectrometer through an image lens (IL). The two-dimensional signal in the y direction of human skin and the spectrum are obtained by a spectroscopy and

two-dimensional CCD. We adopt SD-OCT in this system. The optical power of the detected interference light is expressed as follows: [37,38]

$$I(k) = I_r(k) + 2\sqrt{I_s(k)I_r(k)} \sum_n \alpha_n \cos(kz_n) + I_s(k) \quad (35)$$

where $I_s(k)$ and $I_r(k)$ are the wavenumber-dependent intensities of the sample and reference light beams, respectively, and k is the wavenumber. The second term on the right-hand side of Eq. (35) represents the interference between the sample and reference light beams. α_n is the square root of the sample reflectivity at the depth z_n . The information in the depth direction of the sample is obtained by an inverse Fourier transform of Eq. (35) as

$$\left| FT^{-1}[I(k)] \right|^2 = I^2(z) \otimes \left\{ \delta(0) + \sum_n \alpha_n^2 \delta(z - z_n) + \sum_n \alpha_n^2 \delta(z + z_n) + O[I_s^2/I_r^2] \right\} \quad (36)$$

where $I(z)$ represents the envelope of the coherence function of the light source. The first term in the curly braces expresses the autocorrelation function of the reference light. The second and third terms express the interference of the sample light and reference light, which gives us information related to the depth direction in the sample. The fourth term expresses the autocorrelation function noise. The system consisting of SD-OCT with multicylindrical lenses allows to obtain a single image by a one-shot measurement whose time is only a few dozens of milliseconds. Therefore, the SD-OCT system can obtain a tomogram of human skin nondestructively and noninvasively.

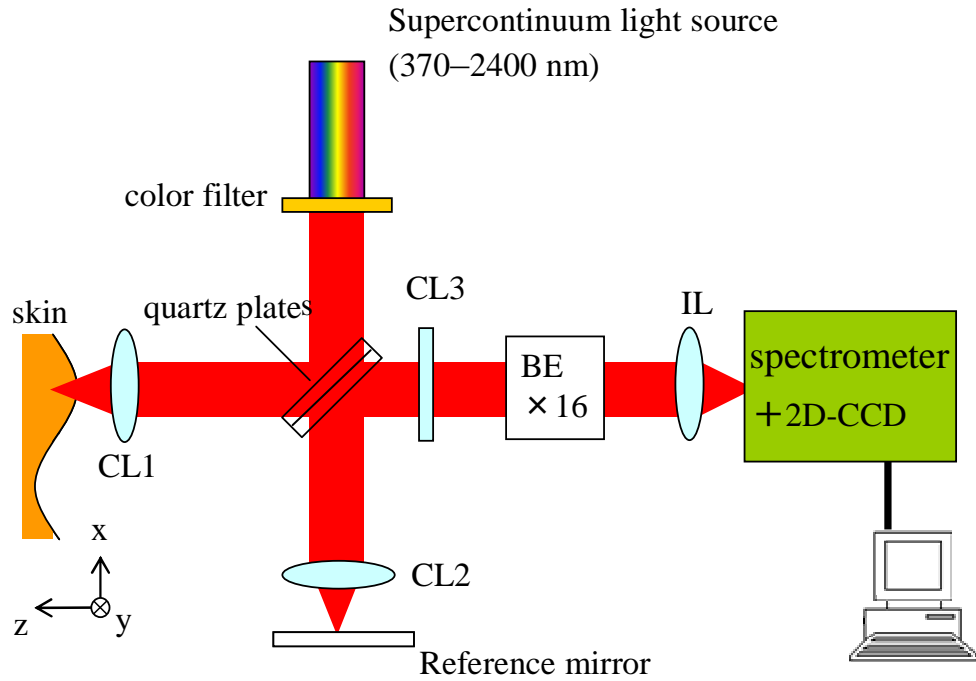


Fig. 9 UV- and visible-light one-shot SD-OCT system.

2) System Performance

Fig. 10 shows the spectrum of light that was used for the OCT measurement of human skin in this study. The wavelengths of the R, G, B, and UV light are 650 ± 20 nm, 550 ± 20 nm, 450 ± 20 nm, and 397 ± 5 nm, respectively. The light intensity is approximately 1 mW/cm^2 for R, G, or B light and approximately $5 \text{ }\mu\text{W/cm}^2$ for UV light. The depth resolution for OCT is given by $2 \times [\ln(2)/\pi] \times (\lambda^2/n\Delta\lambda)$ in theory, where λ is the central wavelength, n is the refractive index, and $\Delta\lambda$ is the spectrum width of the light source. The depth resolution improves as λ is decreased or $\Delta\lambda$ is increased. The theoretical depth resolution in air was $9.3 \text{ }\mu\text{m}$, $6.7 \text{ }\mu\text{m}$, $4.5 \text{ }\mu\text{m}$, and $14 \text{ }\mu\text{m}$ in reference to R light, G light, B light, and UV light, respectively. The transverse resolution was approximately $6 \text{ }\mu\text{m}$, which was acquired from an USAF 1951 resolution target.

2. Result

1) Validation

Fig. 11 shows the absolute-squared interferograms of light, which were obtained by a fast Fourier transform (FFT) of the spectra in Fig. 10. The half bandwidth for peak in air was $7.7 \text{ }\mu\text{m}$ in reference to R light, $5.3 \text{ }\mu\text{m}$ in reference to G light, and $3.6 \text{ }\mu\text{m}$ in reference to B light. I accurately estimated the depth resolution for R, G, and B light almost as planned. As for UV light, the half bandwidth for peak in Fig.11 was $5.0 \text{ }\mu\text{m}$, which was very narrow compared to the theoretical depth resolution. Meanwhile, the bottom of the spectrum in Fig. 11 (d) was broad. This was thought to be due to the deviation in the UV light spectrum in Fig. 10 (d) from ideal Gaussian distribution.

Fig. 12 shows an example measurement of a multilayered film. In Fig. 12 (a), schematic of the film measured is shown and the numbers indicate the boundaries of films. Fig. 12(b) shows a tomographic image of a multilayered film with R light (698 ± 32 nm). The reflection of light from the surface, boundaries, and back side of the film are observed. Assuming that the refractive index of the sample is 1.5, the half bandwidth for the peak in Fig. 12 (c) was estimated to be $\sim 4 \text{ }\mu\text{m}$, which is approximately the same as the theoretical resolution with R light (698 ± 32 nm). The maximum measurement depth was approximately $600 \text{ }\mu\text{m}$ as in Fig. 12 (b). The measurement time was 100 ms on average because the sample did not move during the measurement.

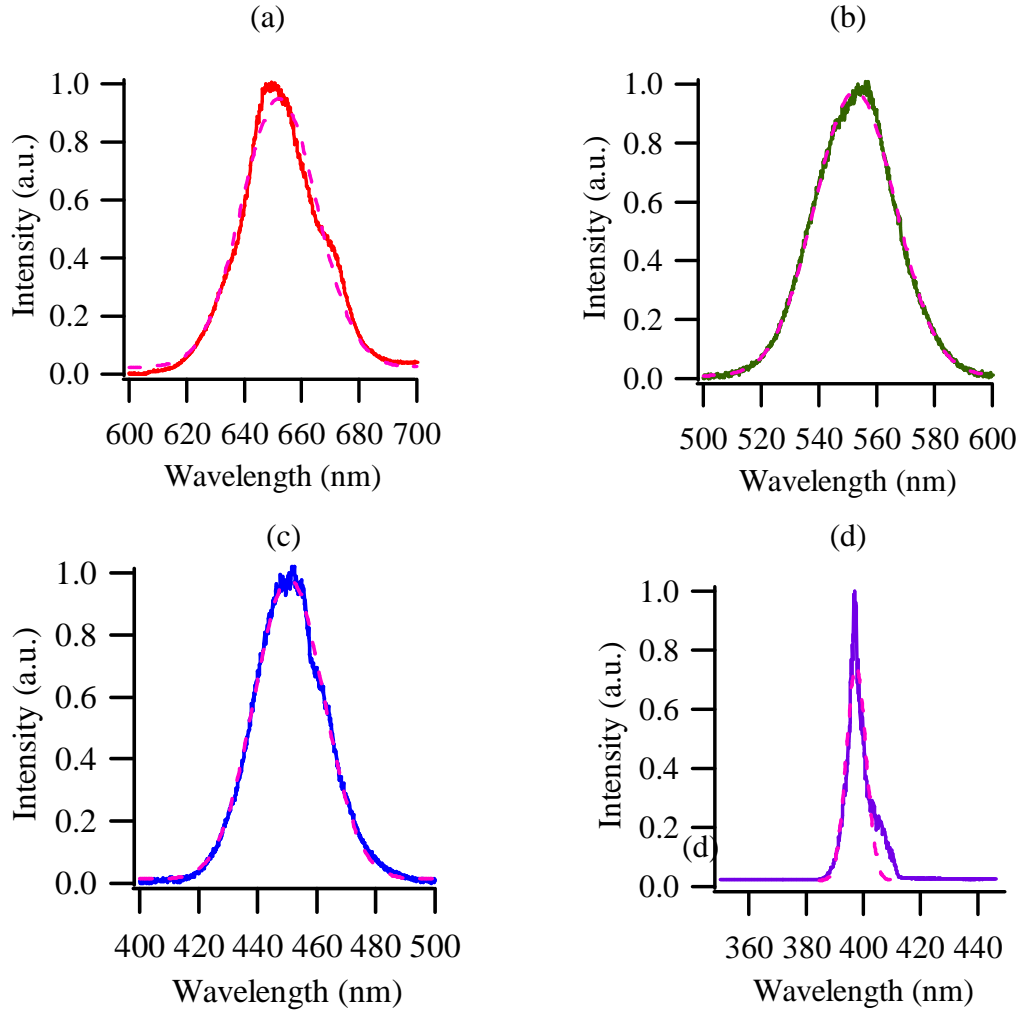


Fig. 10 Light spectra transmitted by a single-color transmittance filter: (a) R, (b) G, (c) B, and (d) UV light. The solid lines show the experimental transmission spectrums measured by V7200 UV-VIS-NIR spectrophotometer (JASCO Co.). The dotted lines represent Gaussian fitting curves.

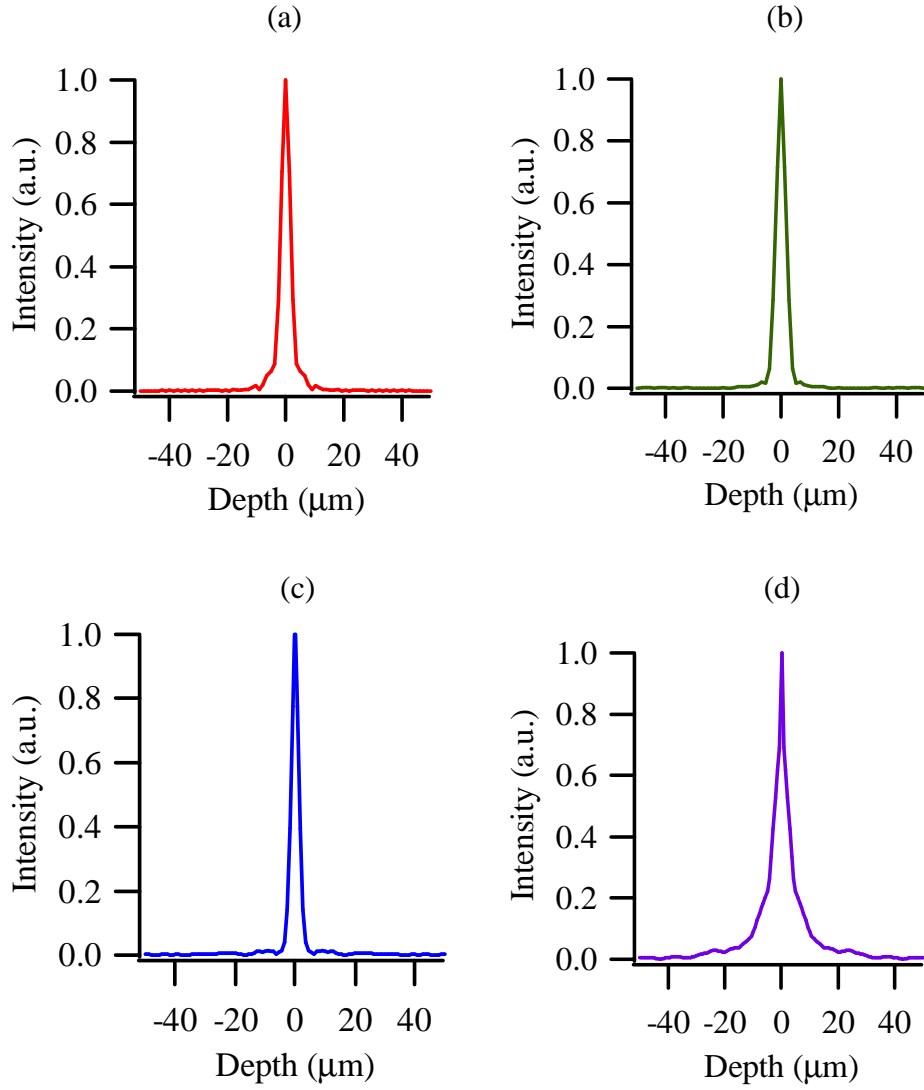


Fig. 11 Absolute-squared interferograms of the light spectra in Fig 2: (a) R, (b) G, (c) B, and (d) UV light.

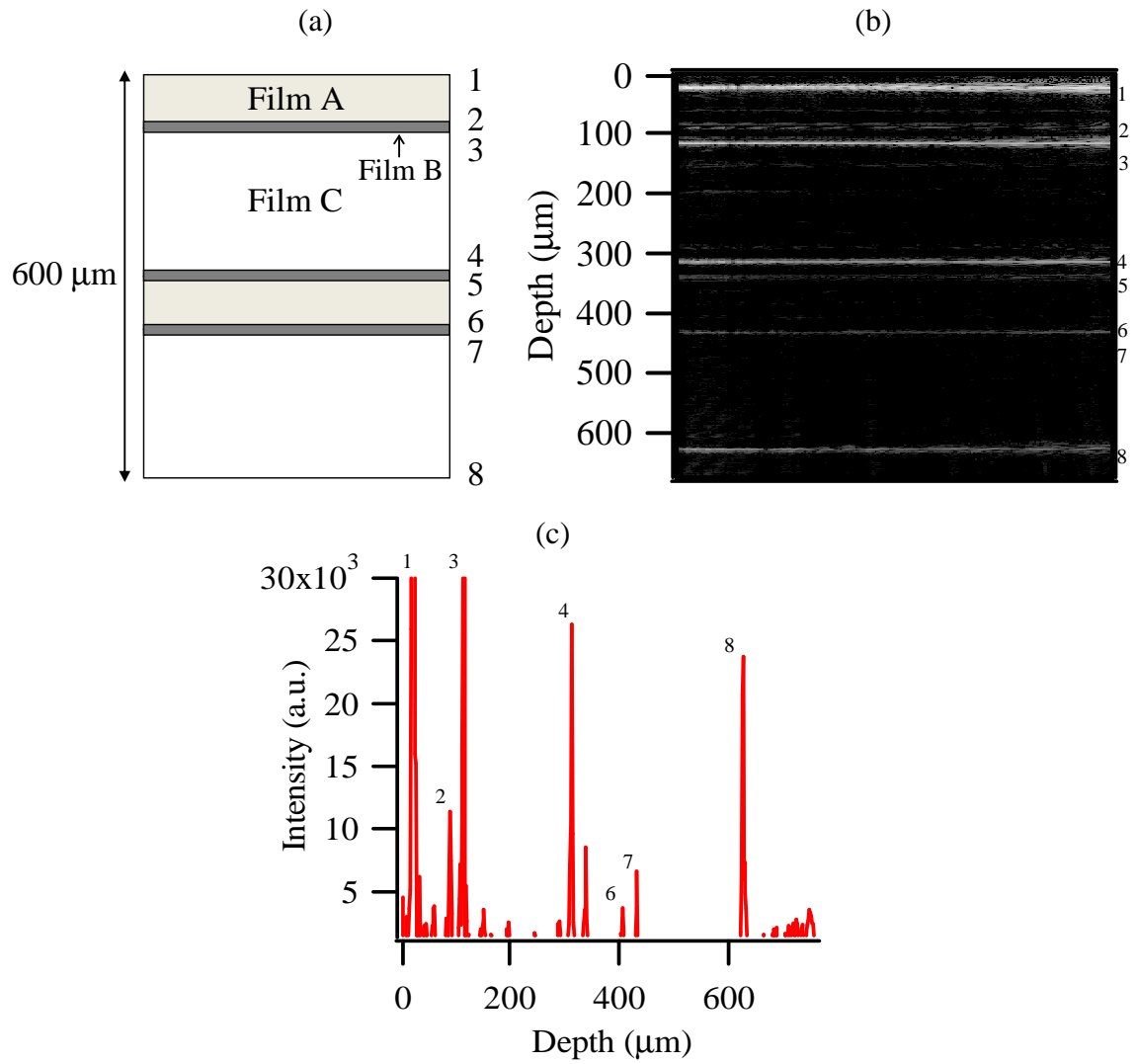


Fig. 12 An observation of a multilayered film. (a) Schematic of the film. The numbers indicate the boundaries. (b) The tomogram of the film. The brightness corresponds to a logarithmic scale. (c) One-dimensional profile of the tomogram.

2) RGB tomography of live human skin

Fig. 13 shows a tomogram of live human skin (the back of the left arm, skin phototype III, 36 years old) for each RGB color. The measurement time was 20 ms. For a comparison of the tomograms of each color, the brightness of each tomogram was divided by the peak intensity of the spectrum of the laser source with each color filter in Fig.14 for normalization. The peak intensities depended on the overall system performance including the intensity of the laser source, the transmittance of the color filter, and the sensitivities of the spectroscopy and detector. In Fig. 13, We can observe an irregularity in the skin surface and the stratum corneum, the epidermis, and the upper layer of the dermis [39]. The imaging depth of R light was greater than 200 μm in Fig. 13 (a). The signal from the dermis is higher than that from the epidermis because of the large scattering of light by fibrous tissue such as collagen in the dermis. The signal of the G light was observed mainly within the depth of approximately 150 μm from the surface of the skin in Fig. 13 (b). The signal of the G light from the dermis was smaller than the signal of the R light from the dermis because G light was absorbed by the hemoglobin in the blood capillaries in the dermis. B light was reflected mainly from a depth of less than 100 μm in Fig. 13 (c). This is mainly because B light is absorbed by the melanin in the epidermis, which has a larger coefficient of absorption in the wavelength region of B light than G and R light. To our knowledge, these are the first tomographic images of live human skin with R, G, and B light. This makes it possible to discuss the differences in the imaging depth of each color. I attributed the differences in the imaging depth to the absorption by the pigment cells in human skin [40,41].

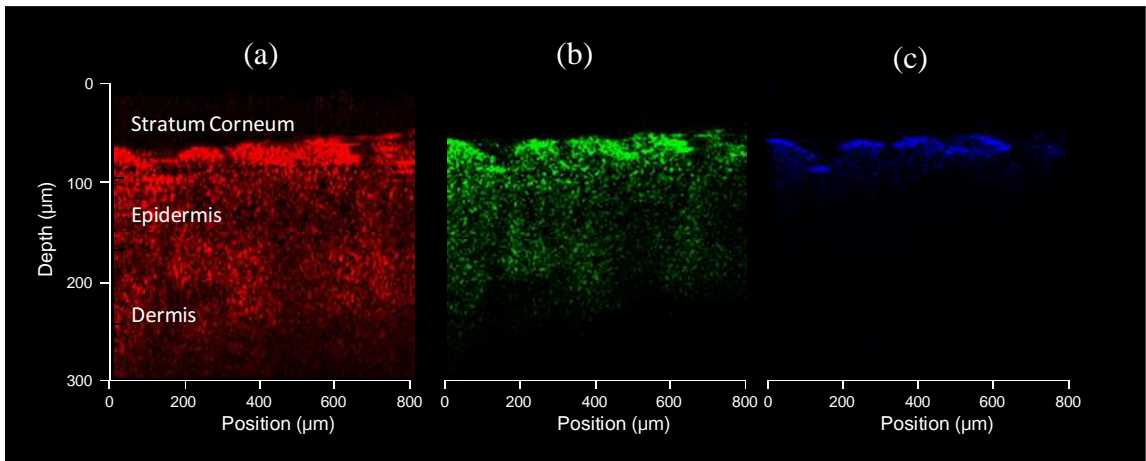


Fig. 13 RGB spectroscopic tomography of live human skin: (a) R light (650 ± 20 nm), (b) G light (550 ± 20 nm), and (c) B light (450 ± 20 nm). The brightness corresponds to a linear scale.

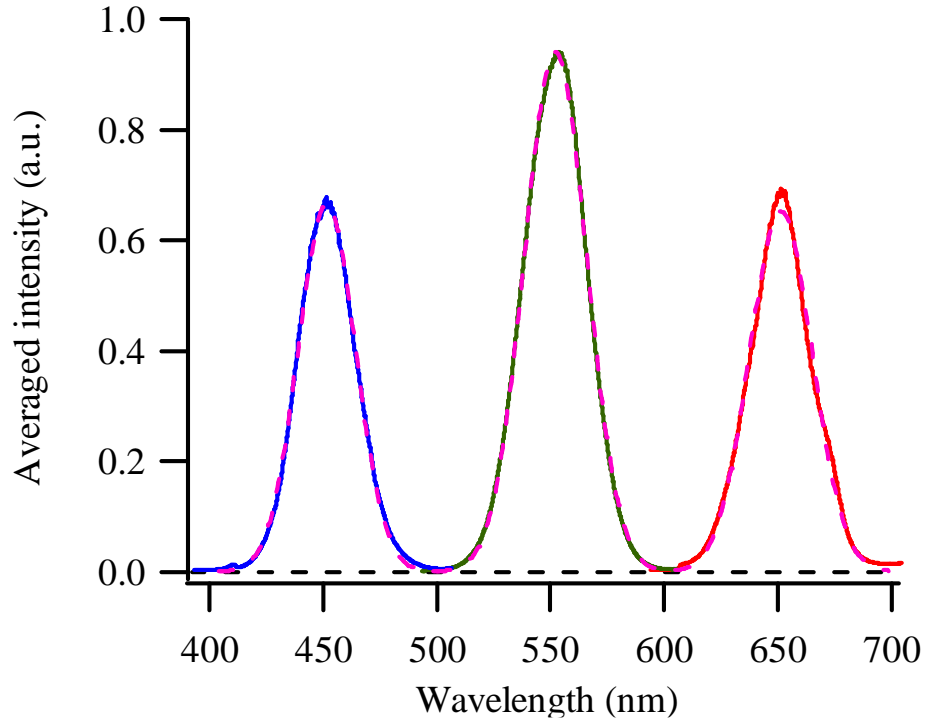


Fig. 14 Spectra of the laser source with each color filter. The intensity of each position (y-direction) was averaged. The dashed line is the Gaussian curve.

R light deeply penetrated the skin and was reflected from various depths in the skin. Therefore, in daily life, R light is considered to make mottled points and wrinkles on the surface of the skin less noticeable by the soft focusing effect in the depth direction. On the other hand, B light was reflected from the skin at more shallow depths. Therefore, B light is considered to emphasize mottled points and wrinkles on the surface of the skin.

3) Relation between reflection spectrum and light propagation in skins

To investigate the relation between the appearance and the light propagation in skins, I compare two participants whose appearances are slightly different (Fig. 15). Observation site is at the back of the arm. Skin photo types are both III (Japanese). Each skin's color in this experiment are express as the $L^*a^*b^*$ color space specified by the International Commission on Illumination (CIE). L^* represents the lightness which value are 0 for black and 100 for white, a^* indicates green for the negative values whereas magenta for positive, and b^* indicates blue for the negative values whereas yellow for the positive. $L^*a^*b^*$ values are calculated form the skin reflection spectrum measured by UV-VIS-NIR spectrometer

(V7200, JASCO). Each CIE $L^*a^*b^*$ are $L^*=65.2$, $a^*=9.5$, $b^*=20.2$ for participant A (pA), $L^*=60.6$, $a^*=11.7$, $b^*=22.5$ for participant B (pB) as in Fig. 15.

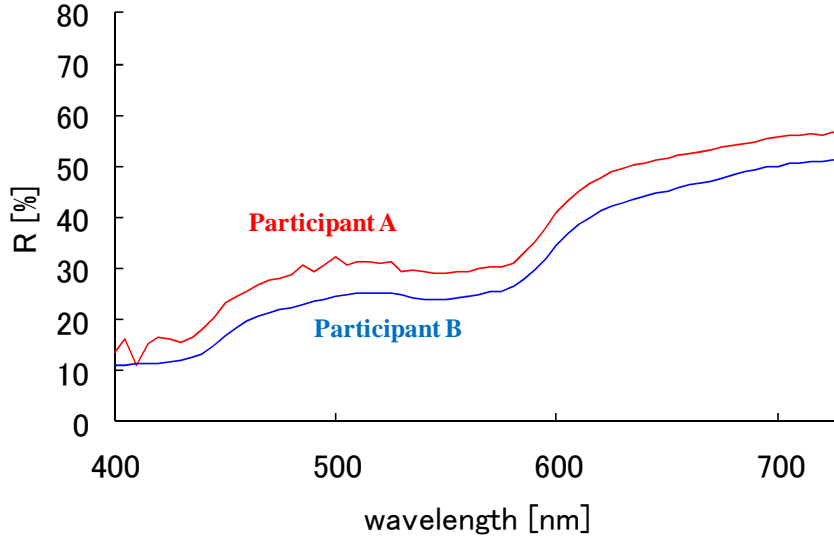


Fig. 15. Reflection spectrums of two participants observed in back of the arm.

Fig. 16 shows the comparison of two human arm skin tomographic images by RGB colors. Observation site is same as the spectrometer in Fig.10. Each images are taken one by one by changing the CFs. As the wavelength become shorter from red to blue, the observation depths become shorter for both pA and pB. This is because green light is absorbed by hemoglobin in dermis and green and blue light are absorbed by melanin in epidermis. This indicates, if someone sees the skin by his or her eyes, although blue light is thus to highlight the surface texture on the skin, the red light is blurring the focus in a depth direction. The observation depths of green and blue for pA are deeper than that for pB. This is correspond to the fact that L^* of pA are greater than that of pB and b^* of pA are smaller than that of pB, i.e. close to blue. Moreover the pA's tendency that observation depths of B and G are smaller than that of R is more prominent than that of pB. This indicates that pA's skin is more redness (a^*) than that of pB. Those results shows that the skin's observation depths of each color are correspond to the color space as the observation depth is decrease so that the light incident to the skin is damping by pigments and cells.

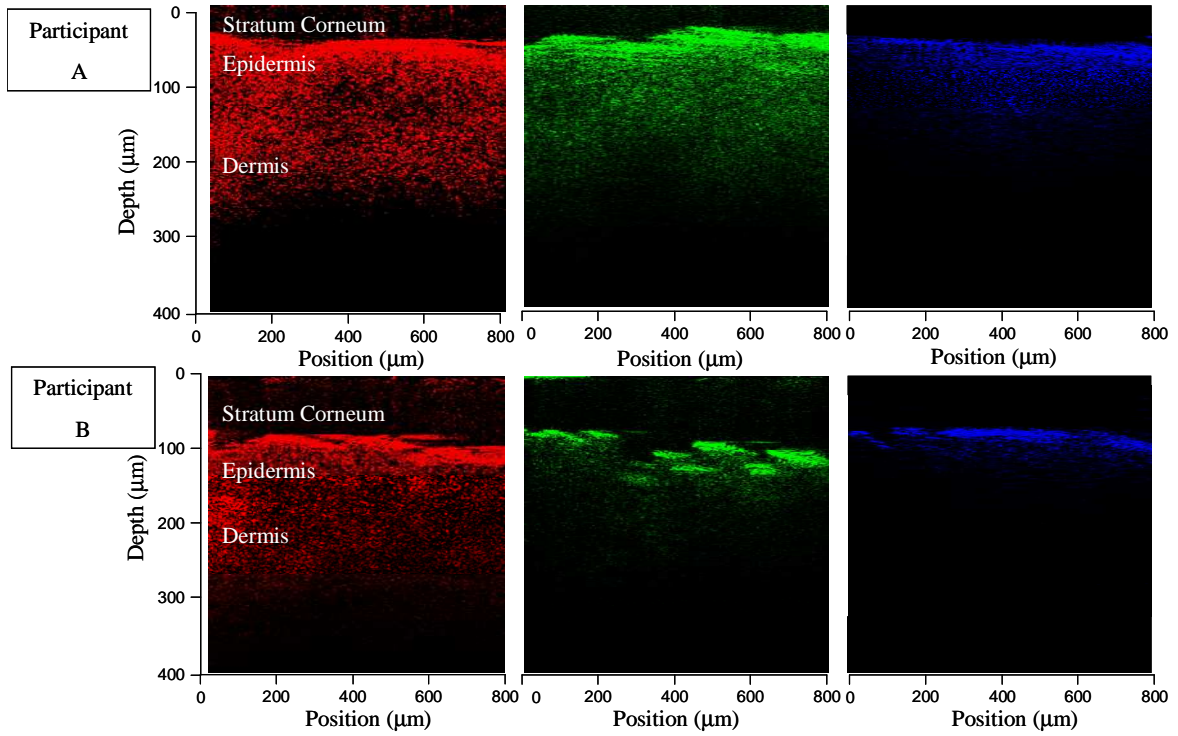


Fig. 16 The living skin tomographic image differences of two participants in RGB, whose skin's reflection spectrums are shown in Fig. 15.

4) Individual differences in transparency of epidermis

Fig. 17 shows skin tomographic images of R color of two different persons. Both skin photo types are both III. Generally, red light is most transparent of RGB colors as absorbance spectrum of melanin and hemoglobin pigment in Red region is small. In fig. 17, one is a 50s men's skin and the another is a 30s woman's skin whose observation depth is especially long relatively. In 50s men's skin, the stratum corneum layer is observed clearly on the top of the skin because the scattering intensity of top layer is strong although that of dermis layer is weak relatively. Thereto in the 30s Woman's skin, the scattering signal of stratum corneum and epidermis layers are weak, but the signal intensity of dermis layer is strong relatively. This experimental result shows that the transparency of the stratum corneum and epidermis layers affects the observation depth. If I peel stratum corneum for dermatology, the observation depth might be much deeper than this skin experiment. This indicated that the observation depth is determined by not only pigment cells but also scattering by cells and disorder of the tissues.

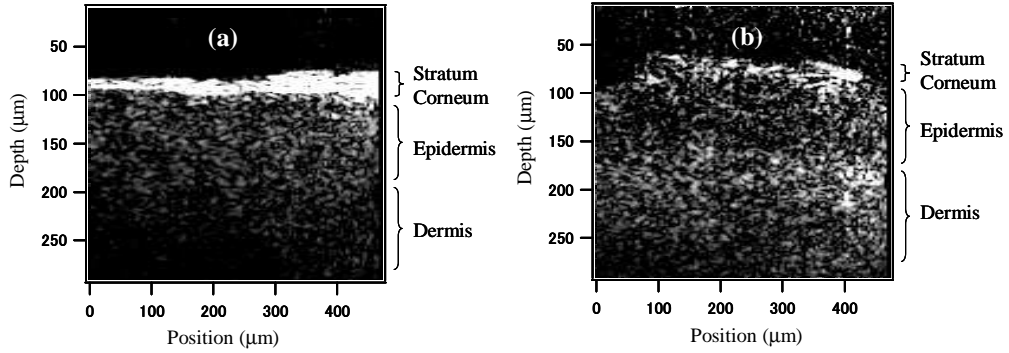


Fig. 17 Difference in tomographic images between (a) 50s men's skin and (b) 30s woman's skin in the back of the arm.

5) UV tomography of a skin excision

The entire protocol was approved by the institutional review board at the FUJIFILM Co. Fig. 18(a) shows a stained skin excision (female, Caucasian, abdomen, 38 years old, BIOPREDIC). The epidermal thickness was approximately 100 μm . A tomogram of the skin excision with UV light ($397 \pm 5 \text{ nm}$) is shown in Fig. 18(b). The locations of measurement in Figs. 18(a) and (b) are different. The intensity of the UV light is much smaller than the visible-light intensity, so I removed the beam expander in Fig. 9 to increase the detected intensity. The resolution in the y direction decreased as the detected intensity increased. I changed the grating of the spectrometer from 1200 L/mm to 2400 L/mm to increase the measurement depth by improving the wavelength resolution. The intensity of the UV light is much smaller than the intensity of sunlight.

In Fig. 18, scattered light from a depth of approximately 200 μm from the surface of the skin was observed. On one subject, I demonstrated that a light in the UV-A (320–400 nm) region reached the dermis with tomography. UV-A light is said to reach the dermis and causes aging such as the appearance of creases [42]. The penetration depth was simulated with various laser wavelengths and skin model types [43,44]. In the simulation, for fair or very fair skin, less than 15% of the UV-A light (365 nm) was simulated to penetrate a depth of 200 μm [44]. The OCT system could detect light that penetrated a depth of 200 μm , decayed to less than 15% in intensity, and scattered back. When the epidermal thickness was assumed to be 100 μm , the relative intensity integrated over the entire dermis and the total amount of backscattered light was calculated to be approximately 20%. The simulated transmittance of the skin heavily depends on the skin type, so I need to measure the various skin types in detail.

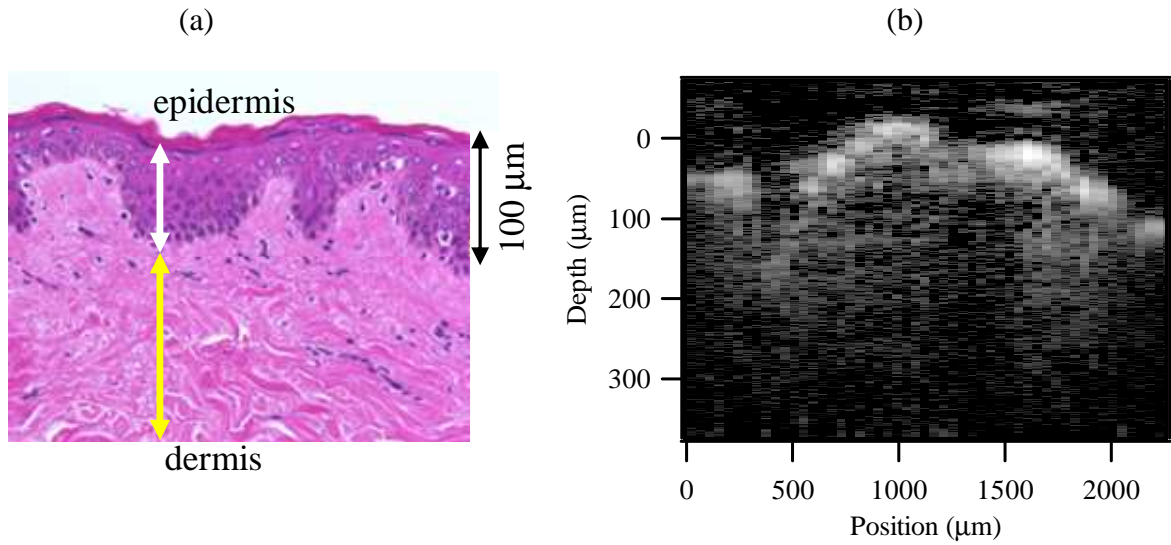


Fig. 18 (a) Stained skin excision photographed with a microscope. (b) Tomogram of the skin excision, which is the same as (a) with UV light (397 ± 5 nm). Each Fig. (a) and (b) is the same human abdomen skin but the locations of measurement for (a) and (b) are different. The brightness corresponds to a logarithmic scale.

3. Conclusion

I developed one-shot SD-OCT that allows for nondestructive observation of a tomogram of human skin for each wavelength region of the UV–visible-light (370–800 nm) spectrum. OCT images of human skin for R, G, B, and UV light were measured. In the visible-light spectrum, R light penetrated the skin and was reflected from a lower depth than G or B light. R light is considered to make mottled points and wrinkles on the surface of the skin less noticeable. On the other hand, B light is considered to emphasize the mottled points and wrinkles on the surface of the skin. On one subject, we demonstrated that UV light (397 ± 5 nm) reached the dermis of the skin with tomography.

The system consists of SD-OCT with multicylindrical lenses; it takes only a few dozens of milliseconds to obtain a single image. Therefore, there is no need to maintain the same measurement point in human skin physically during the measurement. I anticipated that I could evaluate the effect of the application of cosmetics and pharmaceutical products to human skin.

IV Development of full-color OCT and *in situ* measurements of human skin

To nondestructively measure and visualize color below the skin surface that is the root cause of the skin's appearance troubles, I developed full-color optical coherence tomography (OCT). For color reproduction, I developed one-shot spectral domain OCT by using a trichromatic RGB multi band color filter and three spectral detectors. I visualized the difference between color tomograms of the dermis of human skin parts, back of arms and cheeks, and measured the difference based on the extinction coefficient of full-color OCT. Both measurements showed that the inner cheek skin color of UV-exposed areas is yellower and darker than back or arm skin.

1. Method

1) UV-Vis OS SD-OCT and Full-color OCT with trichromatic RGB band pass filter

Fig.19 shows the schematic diagram of UV-Vis OS SD-OCT [45-47]. The supercontinuum laser source (SC400, Fianium Ltd.) generates a broadband white light beam with a wavelength range of 370–2400 nm. The light beam passes through a CF, which is used to shape the light spectrum in the proper manner. The beam is divided into two beams by a quartz plate. The reflected beam is a sample beam that is irradiated to the sample passing through an achromatic cylindrical lens (CL1) so that the light beam is linearly focused on a sample, i.e. skin surface. The transmitted beam is the reference beam. The skin absorbs and scatters the sample beam, then the scattered light passes through the CL1 and the quartz plate and interferes with reference beam reflected by the mirror. The UV-Vis OS SD-OCT system is designed in consideration of the symmetry of the optical paths. The scattered light from the skin sample takes an image on a two-dimensional charge-coupled device (CCD) (255 x 1024 pixels, DU920-BR-DD, ANDOR Technology) by the CL1 and a CL3 that is perpendicular to the curvature direction of lens CL1 which work as an objective lens together and an image lens. A beam expander sets after CL3 to expand an image to 16x magnification. The two-dimensional signal in the y direction of the skin sample and the spectrum provided by the image spectrometer (600 lines/mm 500 nm blaze, MS2001) is obtained and sent to the PC. In this report, I discuss the visible light region; skin images in the UV region are discussed in other reports [47]. The depth resolution, Δl , for OCT imaging in free space is given by

$$\Delta l = \frac{2 \ln 2 / \pi}{\Delta \lambda / \lambda_0^2} \quad (37)$$

where $\Delta \lambda$ is the full width half maximum (FWHM) of the bandwidth of the light beam spectrum after passing through a CF, and λ_0 is the center wavelength [22]. The center wavelength and the FWHM for measurements are 450 ± 20 nm for blue (B), 550 ± 20 nm for green (G), and 650 ± 20 nm for red (R). The depth resolutions given by Eq. (37) are $3.6 \mu\text{m}$ for R, $5.3 \mu\text{m}$ for G, and $7.7 \mu\text{m}$ for B. The beam spectrum was shaped by a trichromatic RGB band pass filter composed of a multilayer dielectric film. The light intensity is 1 mW/cm^2 for R, G, B lights. The transverse resolution, which was acquired from an USAF 1951 resolution target, was approximately $6 \mu\text{m}$.

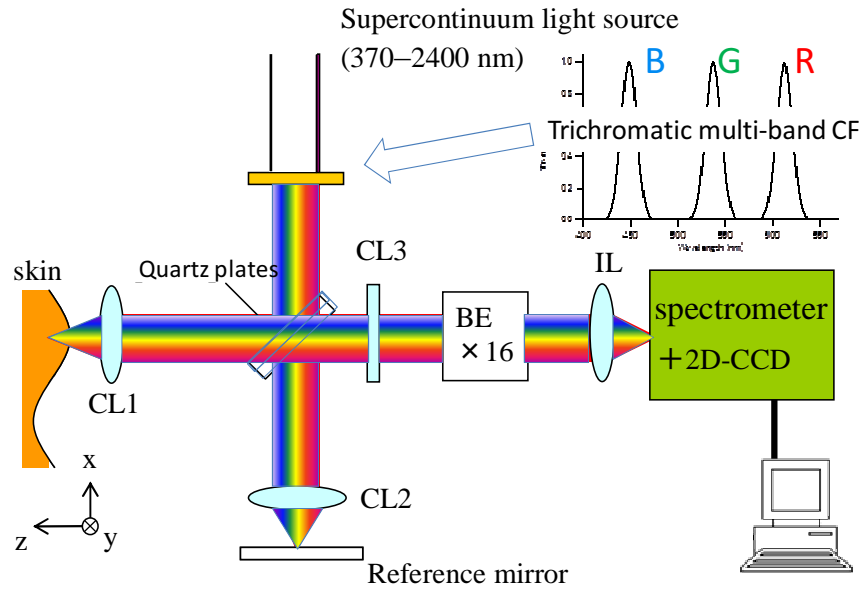


Fig. 19 Schematic diagram of UV-Vis OS SD-OCT with Trichromatic multiband CF. FSP: fused silica plate, CL: Cylindrical Lens, S: sample, M: mirror, OL: objective Lens, IL: image Lens, PC: personal computer

Fig. 20 shows the schematic diagram of full-color OCT. The source and illuminator of a sample and the reference arm are same as that shown in Fig. 19. The light beam passes through the trichromatic RGB band pass filter for which the wavelengths of R, G, and B are 610 ± 20 nm, 540 ± 20 nm, and 450 ± 20 nm, respectively (Fig. 21). The reason for adapting these center wavelengths is to eliminate the effect of color rendering. In general, there is a

plurality of wavelength spectra which can be consider as white, but it is known that these three wavelengths always have a constant intensity ratio [48]. In Fig.20, detections are performed for each color using two dichroic mirrors and three spectrometers (2400 lines/mm 500 nm blaze MS2001 for R, 2400 lines/mm 400 nm MS2001 for G, 1800 lines /mm 450 nm SR500i for B) and CCDs (255×1024 pixels: DU-920-BR-DD for R, 127×1024: DU401-BV for G, 200×1600 DU970N-UVB for B, ANDOR Technology). Three spectral detectors were synchronized. As a basic preliminary experiment, the OCT measurement was performed while moving the standard aluminum mirror in the depth direction, thereby correcting the depth dependence of the light intensity based on the focal depth characteristics of the lens. Interpolation for matching the RGB pixels was executed because each RGB image had a different resolution. For the signal-to-noise improvement of each pixel, we averaged several neighboring pixels. Then, we applied a weight to each color image using a color matching function. Subsequently, each color was converted to 256 gradations and colorized.

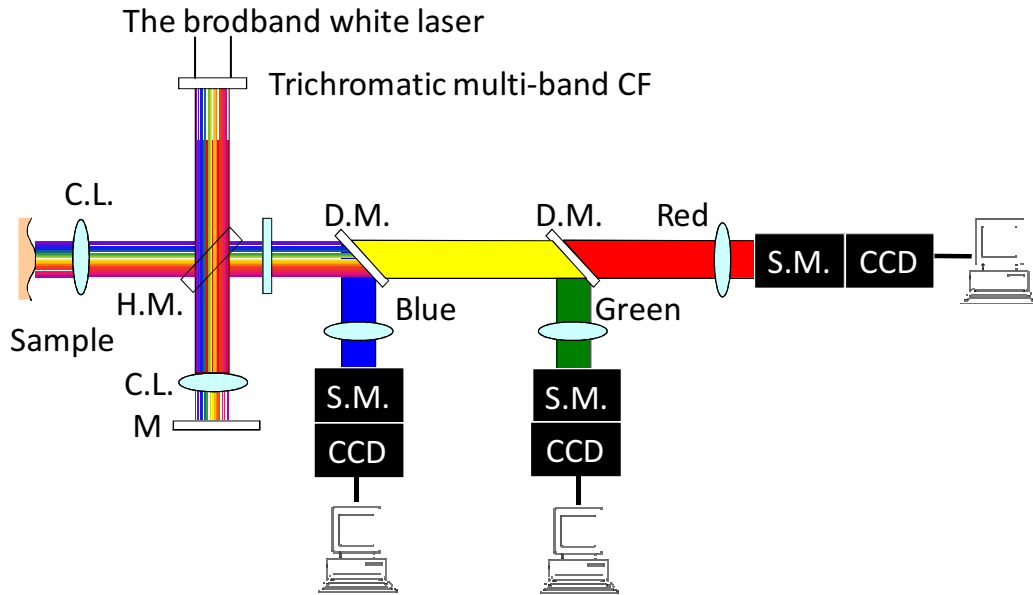


Fig. 20 Schematic diagram of full-color OCT. CF: color filter, H.M.: half mirror, C.L.: Cylindrical Lens, M: mirror, D.M.: dichroic mirror, S.M.: Spectrometer, CCD: charge-coupled device

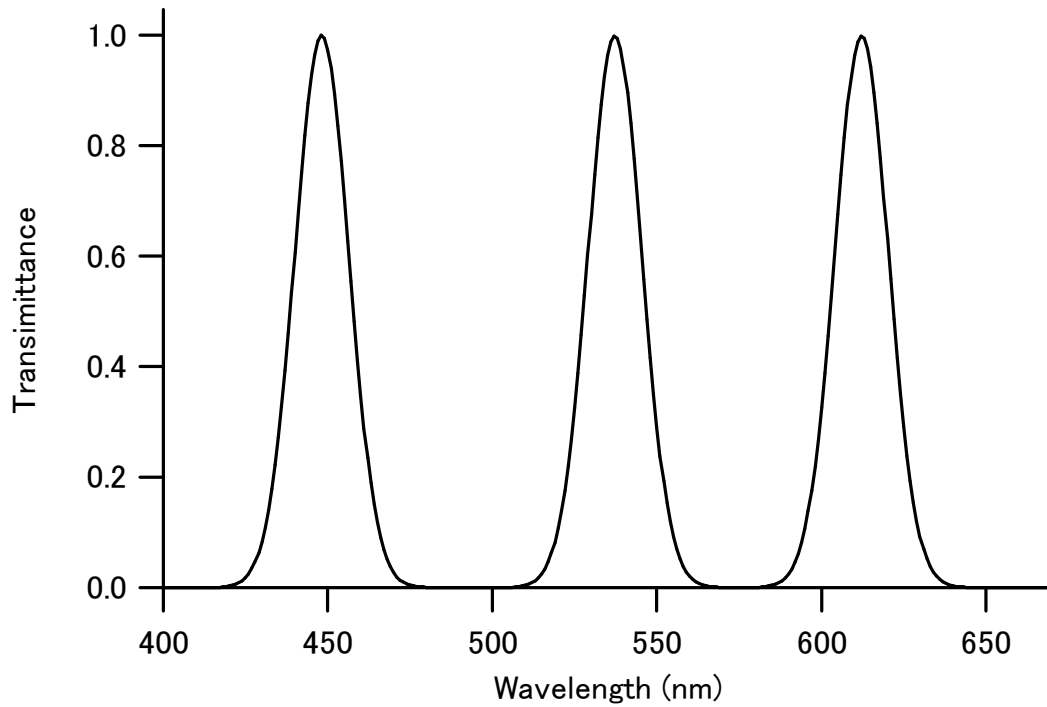


Fig. 21 A full color OCT incident light spectrum measure by V7200 Spectrophotometer (Jasco Co.).

2. Result

First, we examined a simultaneous measurement of RGB colors by using a trichromatic multi-band color filter (CF). The observation site is located at the back of the arm whose skin photo types are both III (Japanese). In Fig. 22, as the shape of outermost surface of RGB is all same, I can confirm the measurement is done at the same time and same position correctly. The observation depth of a multi-band CF measurement is shorter than a single-color measurement because the resolution of the wavelength is decreased to spread the observed wavelength region from one color to three primary colors on the same CCD. A multi-band CF is effective for simultaneous RGB observation, but the penetration depth is not sufficient, especially for the color blue. Thus, we confirmed that the color information obtained from the dermis layer of arm skin was not sufficient to be detected by this system.

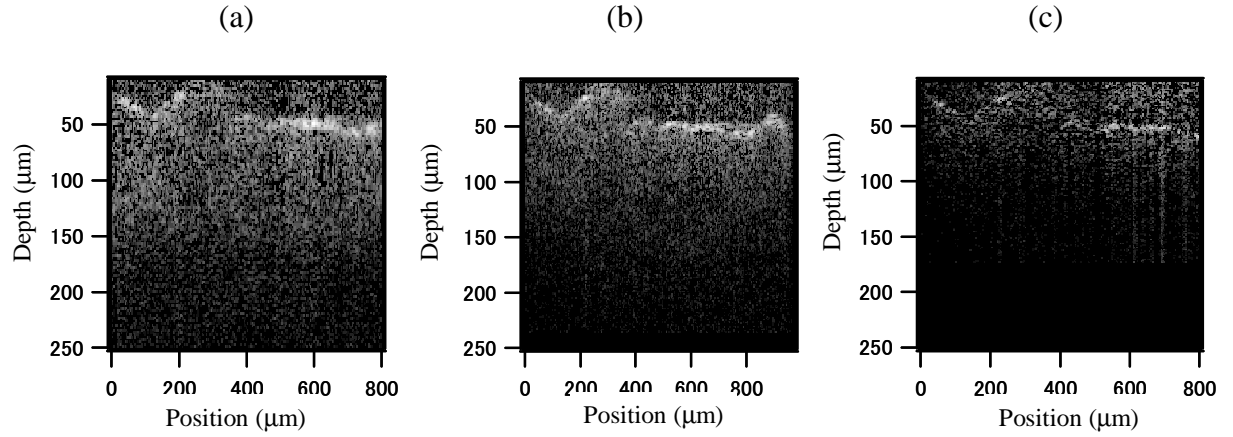


Fig. 22 Simultaneous tomographic images of human skin in RGB colors by multi band CF (a) R, (b) G, (c) B.

Fig. 23 shows the full-color measurement results of two single-color standard samples. A white standard sample was prepared by mixing gelatin with Polystylen (PS) particles and cooling gel, and a yellow standard sample was prepared by mixing PS particles and yellow pigment. As shown in Fig. 23 (a), white was reproduced exactly as a whole. From Fig. 23 (b), in the yellow model sample, the interior is yellow, but the surface is white. The reason why the surface appears white in Fig. 23 (b) is thought to be that the influence of diffusion reflection by PS particles is larger than the influence of absorption on the surface. It was confirmed that the color reproduction is performed correctly by this method.

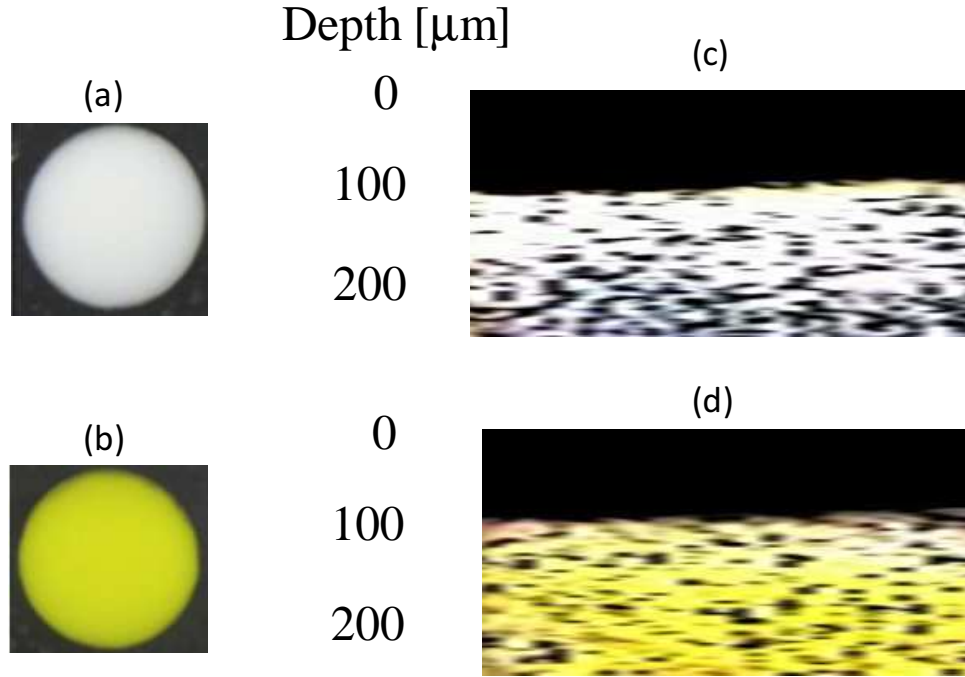


Fig. 23 Color tomograms of single-color standard samples (a) top-view picture of white gelatin by a digital camera, (b) picture of yellow gelatin, (c) color tomogram of white gelatin, (d) color tomogram of yellow gelatin.

Fig. 24 shows color tomograms of the same human skin for each part as obtained by full-color OCT. The decay rate of the epidermis was determined from the average tomographic profile of each wavelength (Fig. 24 (a)). The RGB values of each wavelength in the dermis are recalculated by the attenuation amount obtained from the decay rate. In this analysis, it is assumed that skin is strong scattering medium that is not transparent. Fig. 24 (b) shows the back of the arm and Fig. 24 (c) shows the cheek that is exposed to stronger environmental stressed such as ultraviolet exposure relatively than the back of arm. The cheek tomogram color in the dermis region was darker and slightly more yellow than that in the arm region. This was statistically shown by the RGB extinction coefficients of the dermis in Fig. 25. The z axis is normalized by the mean R value of the backside of the arm. In Fig. 25, the RG values are the same, but B value is different. This also demonstrates that cheek skin exposed to UV-rays is yellower and darker than skin on the inner back arm according to stronger scattering and absorption of blue light in dermis. Several skin changes in dermis layer alterations, such as collagen degradation and decreased collagen synthesis, are considered to occur in response to UV irradiation [6].

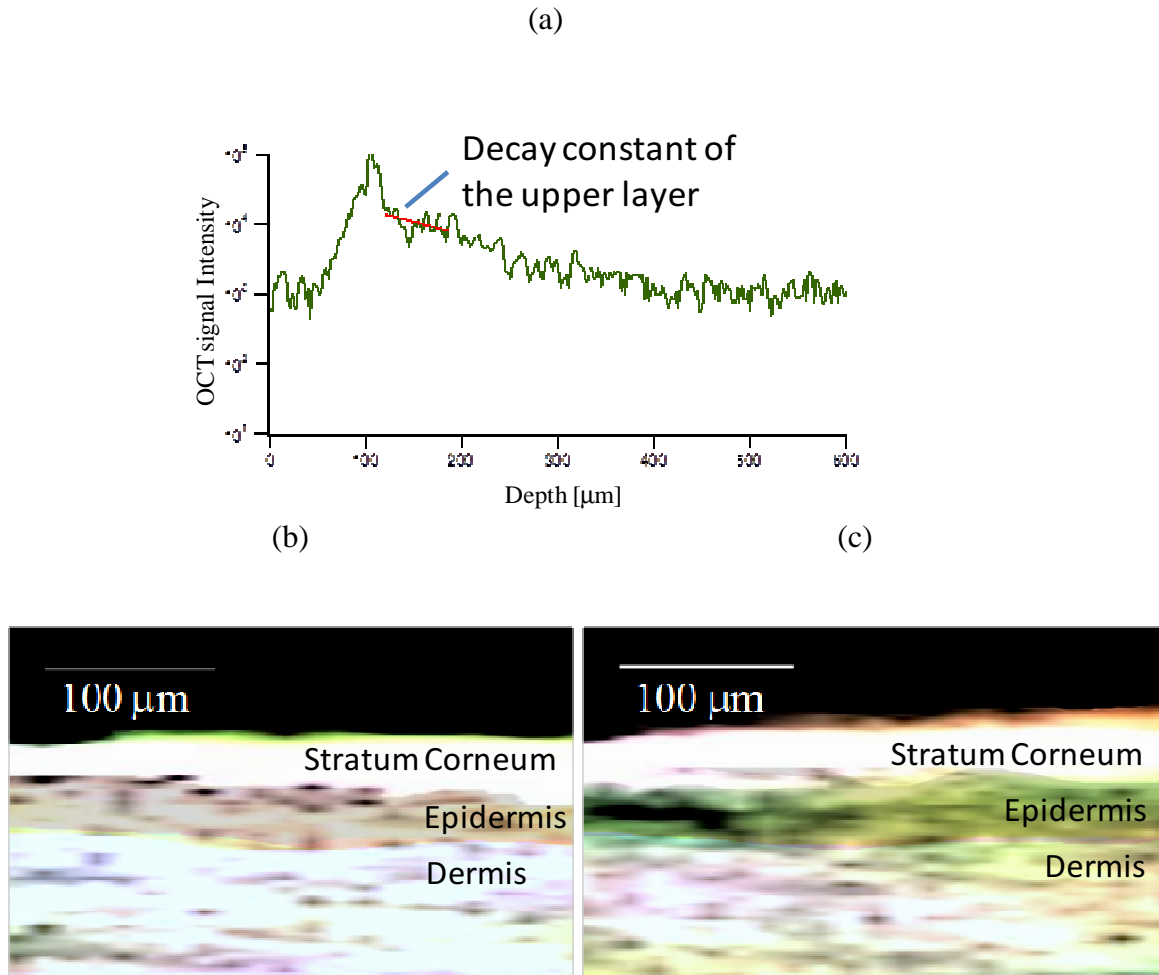


Fig. 24 Color tomograms of a human skin sample. (a) The average tomographic profile. (b) Back of arm. (c) Cheek.

3. Conclusion

I demonstrated simultaneous RGB color measurement by using a trichromatic multi-band CF and three detectors. I developed a method to create a full-color tomogram and applied our method to a model using white/yellow samples. Further, I developed a method to achieve real-color compensation of the lower layer of human skin, which is altered by the influence of the upper layer, and applied our method to human skin. I could visualize the color because of differences in the internal parts of the human skin, and I compared the difference with the extinction coefficient of the dermis. Both measurements showed the same trend; that is, the dermis in the cheek was yellower and darker than the skin on the inner back arm.

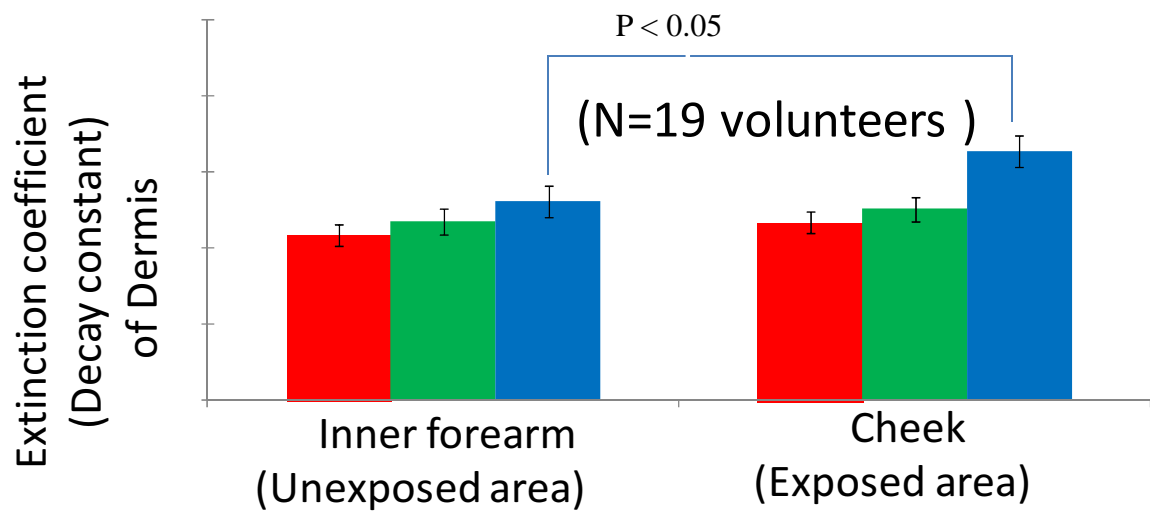


Fig. 25 Difference between skin extinction coefficient in the dermis of inner forearms and cheeks. Red, green and blue bars indicate wavelengths 610 ± 20 , 540 ± 20 , and 450 ± 20 nm, respectively. P-value (<0.05) indicates a significant difference of blue's extinction value in dermis between inner forearms and cheeks.

V Development of high-sensitivity low-coherence dynamic light scattering and determinations of particle size distribution and diffusion motion modes applied to dense particle suspensions

Low-coherence dynamic light scattering systems were investigated to attain a highly accurate measurement of particle size distributions that contained particles of sizes ranging from several micrometers to nanometers in diameter, and to understand the mode of motion in a highly concentrated dispersed particle solution. I have developed a low coherence dynamic light scattering system by combining a microscopic optical system for efficient detection of scattered light into a Mach-Zehnder interferometer using single-mode (SM) fibers. Hereby, the particle size distribution of polystyrene (PS) particles up to 10 nm in diameter could be measured. By changing the microscopic optical system to the immersion fiber probe, it was possible to measure particles up to several nm in 10 μL of solution. By developing an angle-resolved SM-fiber probe system, we clarified that the motion of a PS in a dispersion system is translational motion.

1. Method

1) Principle of LC-DLS

The diffusion constant D and diameter d of the particles in the suspension can be expressed using the Stokes–Einstein relation [24]:

$$D = k_B T / 3\pi\eta d \quad (38)$$

where k_B is the Boltzmann constant, T is the absolute temperature, and η is the viscosity. The power spectrum $P(\omega)$ of a single beam scattered by dispersed particles [49] is

$$P(\omega) = \frac{Dq^2}{\omega^2 + (Dq)^2} \quad (39)$$

where D is the diffusion coefficient and q is the scattering vector.

The power spectrum $P_I(\omega)$ of the signal from the interference between the reference and scattered beams is

$$P_I(\omega) = 2\pi(I_r^2 + 2I_r I_s + I_s^2)\delta(\omega) + \left(\langle I_s^2(t) \rangle_t - I_s^2\right)p_{I_s}(\omega) + 2I_r \int_0^\omega I_s p(\omega, s) \left| \gamma_r\left(\frac{2l_2 + s - 2l_1}{c}\right) \right|^2 ds, \quad (40)$$

where ω is the angular frequency, I_r and I_s are the intensities of the reference light and the scattered light respectively, $\langle \cdots \rangle_t$ represents an average over time, and p_{I_s} and p are the intensity of the scattered light and the power spectrum of the electric field. l_1 , l_2 , and s are the propagation distance of the reference beam, the propagation distance excluding the scattering medium of the sample beam, and the propagation distance of beams scattered more than once in the medium [50]. Also,

$$l_1 = l_2 + s, \quad (41)$$

γ_r is the coherence function of the light source and becomes 0 when the difference between the left and right sides of Eq. (41) is longer than the coherence length of the light source.

The first term on the right side of Expression (40) is the value of the delta function that appears at a frequency of 0. The second and third terms are proportional to the intensity of the scattered light and the power spectrum of the electric field, respectively. Modulation of I_s by the heterodyne method allows us to obtain the component of the power spectrum of the third term to be equal to the power spectrum $P(\omega)$ of singly scattered beams, by extracting and setting s in Equation (41) to within the distance over which single scattering events occur.

With the introduction of the distribution of diffusion coefficients, $f(D)$, in the polydispersed state, Equation (39) becomes

$$P(\omega) = \int f(D) \frac{Dq^2}{(\omega)^2 + (Dq)^2} dD. \quad (42)$$

The autocorrelation function $g_I(\tau)$ is obtained by converting $P(\omega)$ of Expression (8) from the frequency domain to the time domain, as in Equation (9).

$$g_I(\tau) = \int_0^\infty f(D) \cdot \exp(-q^2 D \tau) dD. \quad (43)$$

The particle-size distribution $f(d)$ is then estimated from $g_I(\tau)$ using sampling, histograms, and the CONTIN method. Histogram method minimize error χ^2 with W as variable,

$$\chi^2(\alpha) = g^{(1)}(\tau) - \sum_i^N W_i \exp(-\Gamma_i \tau), \quad (44)$$

where $\Gamma = q^2 D$. The number of N in eq. (10) is a value determined by a measurer. In the CONTIN method[51,52] that is also very commonly used, a constraint condition is added to eq. (44),

$$\chi^2(\alpha) = \sum_i \frac{1}{\sigma_i^2} \left\{ g^{(1)}(\tau) - \int K(\tau, \Gamma) \omega(\Gamma) d\Gamma \right\} + \alpha \|L\omega(\Gamma)\|, \quad (45)$$

where L represents an operation of differentiation twice to ω , and the operation is weighted by α . The value of α is determined by a measurer and the result of ω and the formula is close to eq. (44) when $\alpha \neq 0$.

2. Result

1) Examination of interference method and irradiation method

A schematic diagram of a Michelson type LC-DLS device based on SLD is shown in Fig. 26 (a). For the light source, a super luminescent diode (SLD, S830-G-I-20 manufactured by Superlum Co.) having a wavelength of 835.7 nm and a full width at a half maximum of 18 nm was used. Light from the light source was divided by a photo coupler at a ratio of 50:50. Half of the divided light was emitted from the fiber and then irradiated as parallel light by the collimating lens to the dispersion liquid and the other half was emitted from the collimating lens to reflect the PZT driven mirror back and forth in the direction of the optical path. The latter half was used as a reference light to which phase modulation was added. The backscattered light from the sample returns to the fiber again and is guided to a detector (NewFocus Model 2007) through a coupler. The scattered light from the sample returns to the fiber again through the collimating lens, and a signal that interferes with the reference light is detected.

The Mach-Zehnder type LC-DLS is shown in Fig. 26(b), and the light from the SLD is divided by a photo coupler at a ratio of 99: 1; 99% of the light was irradiated to the measurement sample through a circulator, and 1% of light was phase-modulated by an electro-optic modulator (EO-PM-NR-C1 manufactured by Thorlabs Co.) to obtain the reference light. The backscattered light from the sample returned to the fiber again and was led to the detector via the circulator. The scattered light was combined to interfere with the reference light by placing a photocoupler in front of the detector. Scattered light was then collected using a microscope objective lens with a magnification of 10 in the Mach-Zehnder type LC-DLS sample optical system (Fig.26(c)).

A turbid suspension of polystyrene (PS) standard particles with a particle diameter of 252 nm was measured using various methods, including Michelson-, Mach-Zehnder-, and

microscopic-type optical systems, and the fluctuation of the scattering light was converted into a power spectrum. The results from comparing the intensity are shown in Fig. 27. Measurement sensitivity was improved by using a Mach-Zehnder type interferometer. The reason for the improvement is that the ratio of the interference light to the non-interference light can be increased by making the reference light intensity somewhat closer to the weak scattered light intensity. Since the incident intensity of the detector has a limit, there is a limit to the method of increasing the incident light intensity. The measurement sensitivity was further improved by making the irradiation system a microscopic optical system. It is because scattered light collection efficiency has been improved by widening the aperture ratio. Furthermore, in this system as Fig. 26(c), by having the fiber act as an aperture, it can be considered the system is a confocal optical system that has a small scattering volume observed effectively. If a Mach-Zehnder type interferometer is combined with a microscopic optical system, such as the Michelson type, it is found that the original signal intensity increases by 1000 times or more (Fig. 27).

The particle size distribution of standard particles was measured with the Mach-Zehnder type LC-DLS system using a microscopic objective lens, as shown in Fig. 26(c). Measurement of polystyrene aqueous dispersion with a volume concentration of 10% and a particle size of 13 nm is shown in Fig. 28(a) and (b). The particle size distribution measured by LC-DLS was statistically processed from photographs taken with a transmission electron microscope (TEM) (Fig. 28(c)). The measurement result for a particle size of 99 nm is shown in Fig. 28(d); LC-DLS and TEM agree with each other. There is no other report that accurately describes the particle size distribution of 10 nm based on the LC-DLS method.

The dispersion state of the sample obtained by mixing the three kinds of polystyrene latex suspensions, with average particle sizes of 23, 59, 99 nm and a volume concentration of 10%, is shown in Fig. 29. The obtained particle size distribution was in good agreement with the results predicted from the transmission electron micrograph and the mixing ratio. From the above, it was found that this method is effective for the quantification of the polydispersed state in real systems.

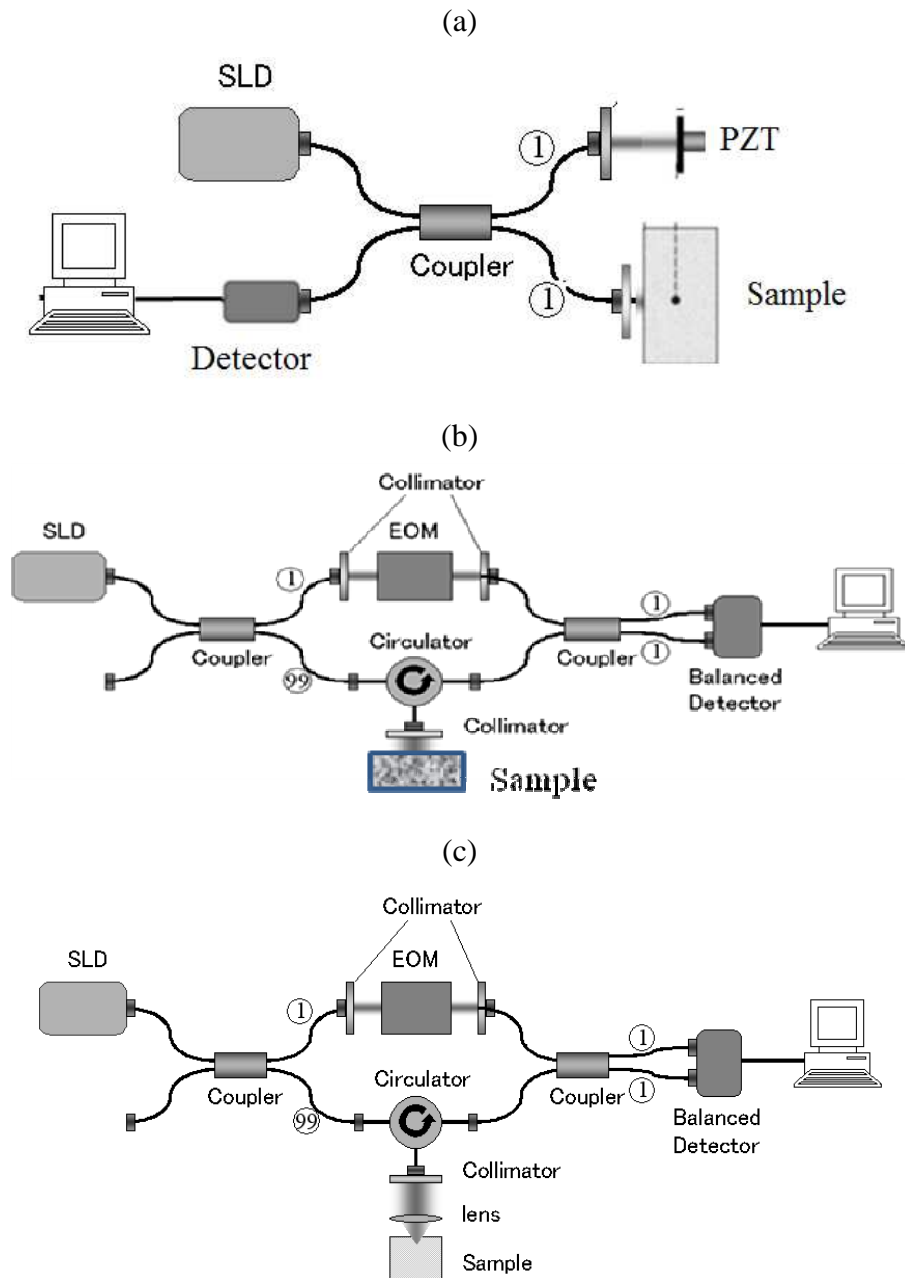


Fig. 26 Comparison of Low-coherence Dynamic Light Scattering Systems: (a) Michelson interferometer, (b) Mazh-Zhender interferometer, and (c) Mazh-Zhender interferometer with confocal optical system.

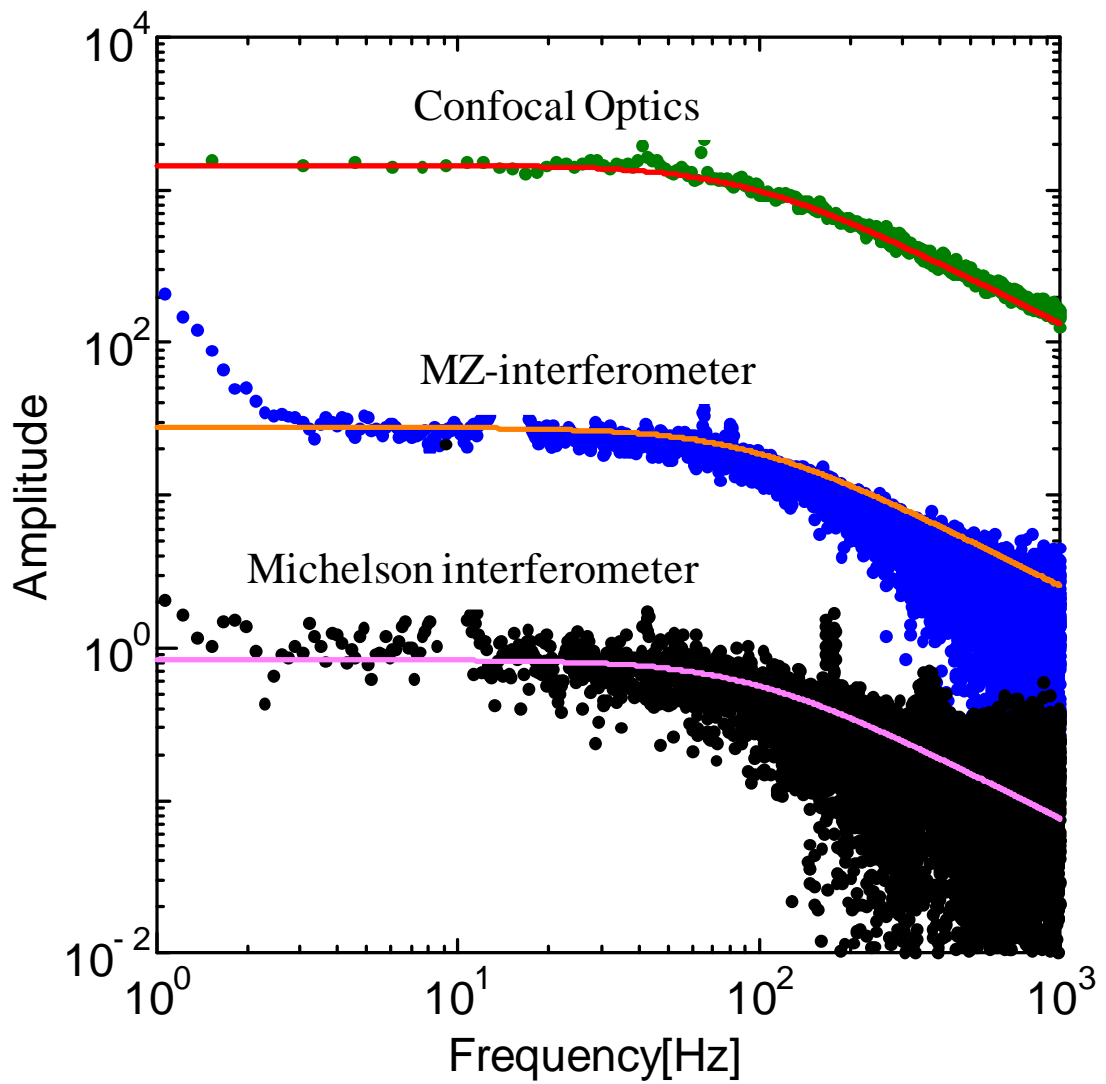


Fig. 27 Comparison of power spectrums of polystyrene suspension (252 nm 10 wt%) measured by different LC-DLS systems shown in Fig.26 (dots: experimental results, solid line: theoretical value of 252 nm particle).

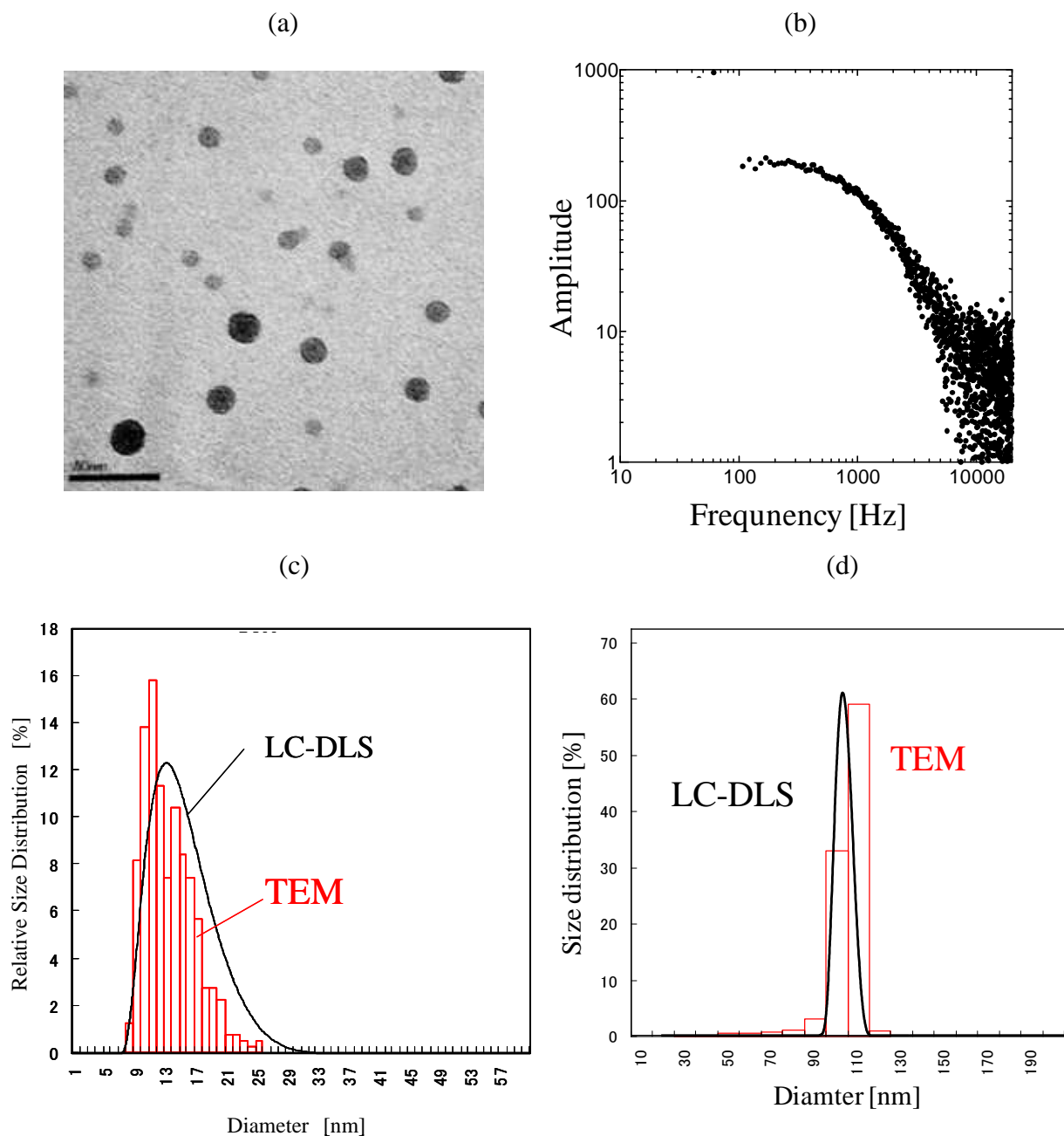


Fig. 28 Particle size distribution of polystyrene suspensions: (a) Transmission electron microscope (TEM) image of 13nm, 10wt% polystyrene suspension (scale is 50 nm). (b) The power spectrum of sample of Fig (a). (c) The size distribution comparison measured by LC-DLS (the curve line) and TEM (the bar graph), and (d) comparison of 99 nm, 10wt% polystyrene.

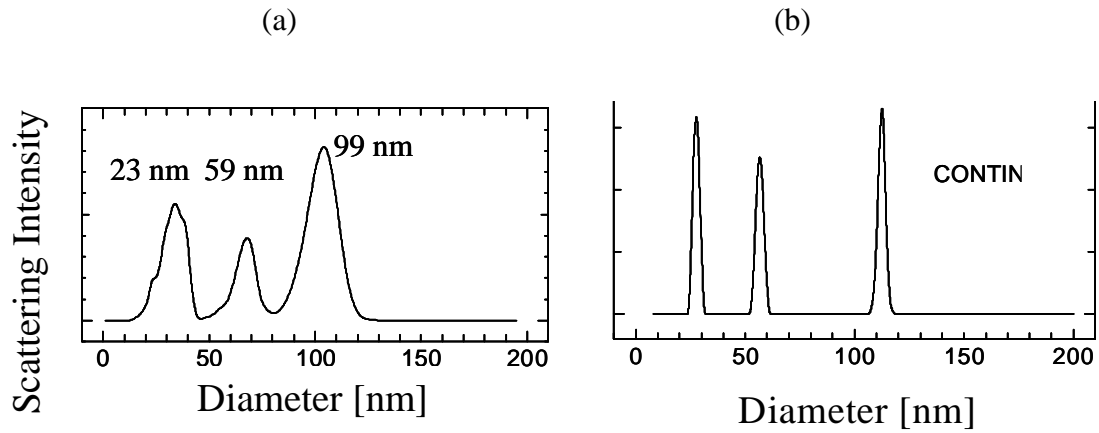


Fig. 29 Particle size distribution of polystyrene mixed suspension of 23, 59, 99 nm size particles, obtained by (a) TEM and mixing ratio and (b) by LC-DLS.

2) Immersion SM-fiber probe

In the analysis of medicines and proteins, because the sample is expensive and valuable, the typical sample size is small. Therefore, we developed a fiber-type trace detection unit (Fig.30). The output of the fiber trace unit is compared with the measurement results of the Mach-Zehnder type microscopic optical system (Fig. 26(c)); the total power spectrum including the homodyne component is shown in Fig. 31. The spectrum, around 0 Hz, on the right side of equation (40) is the homodyne component of the first. The second terms of equation (40), 20 kHz, is the heterodyne component of the scattered light; the harmonic component is 40 kHz. In the fiber dipping type, the noise in the high- frequency range was suppressed. It is speculated that vibration noise of reflected light was suppressed, compared to the system in Fig.26(c) in which an interfacial multiple reflection due to the sample cell existed. It was found that the scattered light can be sufficiently measured even with a small amount of sample. In addition, it was confirmed that particles with an average particle diameter of 2.7 nm were measured [53].

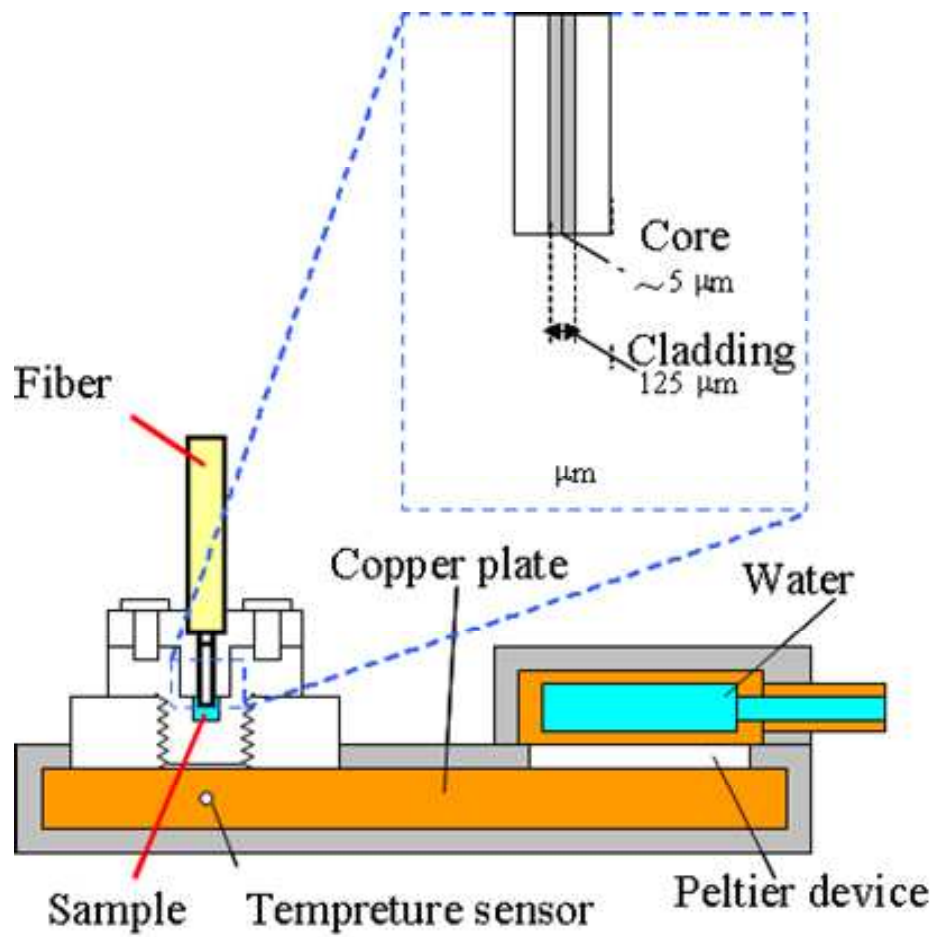


Fig. 30 Experimental setup of SM-fiber probe LC-DLS.

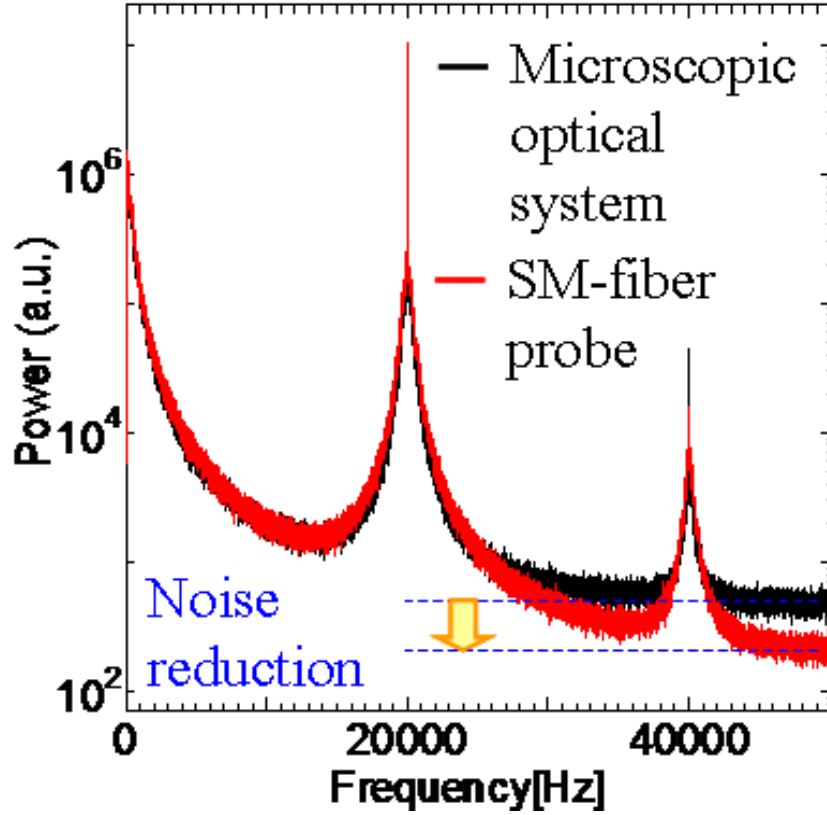


Fig. 31 Comparison of power spectrum of polystyrene suspension (10 %, 100 nm), measured by the microscopic optical system and the SM-fiber probe system.

3) Angle-resolved LC-DLS

It is known that diffusion motion in solution has different modes of motion of crosslinked polymer chains such as rotational diffusion, co-diffusion, and polymer gel, besides translational diffusion due to Brownian motion (Fig. 3). In order to understand the dispersion state that is peculiar to high concentration, it is necessary to discriminate between these modes.

The attenuation constant of the time correlation function, $g_I(\tau)$, is expressed by the equation (7) [54]:

$$\Gamma = q^2 D . \quad (46)$$

Here, Γ indicates the exponent of exponential function in Expression (46). When $q=0$ (i.e. scattering angle $\theta=0$ deg.), the incident direction of light and the scattering direction are the same, hence fluctuation cannot be detected because the light pathlength is the same even if particle positions are different anywhere. On the other hand, when $q=4\pi/\lambda$ (i.e. the

back-scattering direction $\theta=180$ deg.), the fluctuation can be detected because light pathlength difference is twice of their interparticle distance.

In the case of rotational diffusion, when a component of V polarized light is detected after incident H polarized light, a term depending on q (D_t) and the non-dependent term (D_r) [54] is given as follows.

$$\Gamma = q^2 D_t + 6D_r \quad (47)$$

In eq. (47) non-dependent term D_r indicates the rotational diffusion term. When $q=0$, the traveling direction of light and the scattering direction are the same but the rotation mode remains then a diffusion speed of rotation mode can be detected by DLS.

When the dispersion system becomes a gel, there are static components and dynamic components frozen in space, and the attenuation constant varies randomly without dependence on q due to concentration fluctuation. By using the partial heterodyne method proposed by Shibayama, a true diffusion coefficient is obtained [55].

Fig. 32(a) is a schematic diagram of an angle-resolved probe system connected with the LC-DLS Mach-Zehnder which is highly sensitive (Fig.26), because the angle variable measurement is necessary for attribution of diffusion mode. We adopted a method to immerse the fiber directly in the sample. The angle of the two opposite fibers was adjusted with the XYZ translation and two axis goniometer stage that fix these fibers. In order to avoid collision, the result of measuring the dispersion obtained by mixing suspensions of average particle size 99 nm and 755 nm by angle variable LC-DLS is shown Fig. 32(b). This clarifies that translational diffusion is measured because the measured two diffusion coefficients are straight lines passing through the origin.

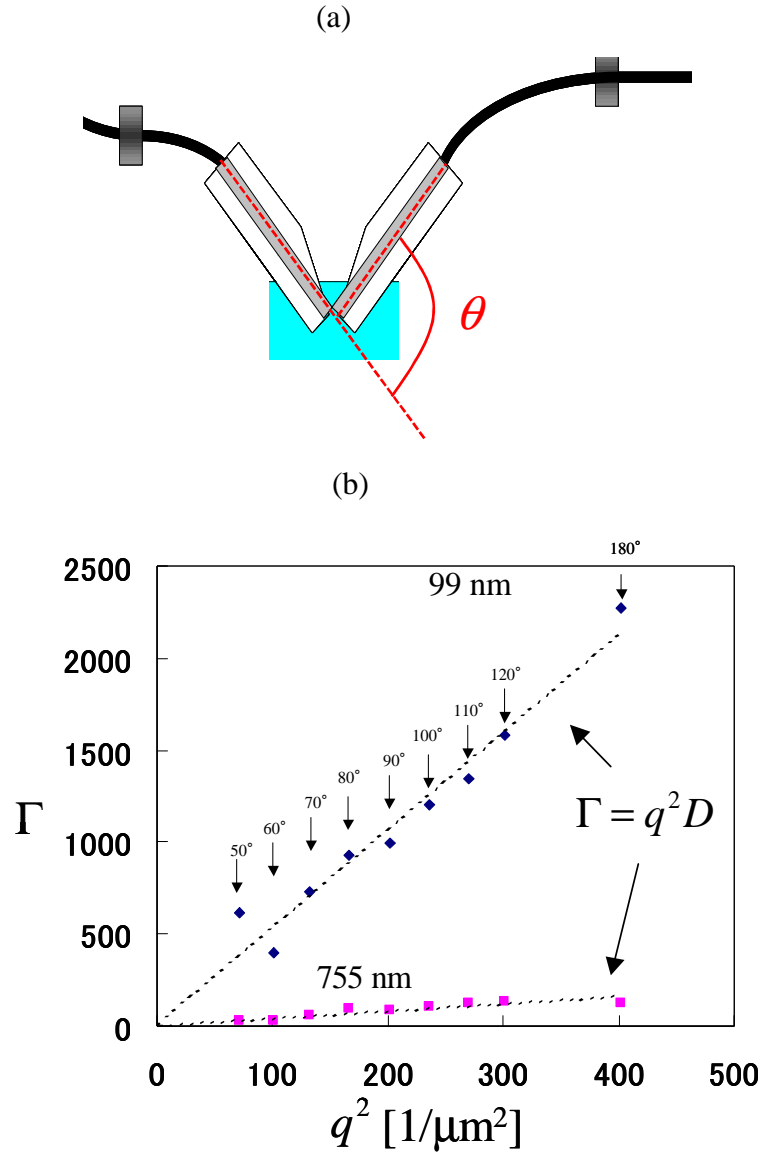


Fig.32 Identification of diffusion modes of polystyrene particles: (a) Angle-Resolved SM-fiber probe system, (b) Translational diffusion mode of polystyrene (10 %, 99 nm and 755 nm). The subscripts numbers indicated by the arrows denote the scattering θ angle defined as fig (a).

3. Conclusion

I developed an LC-DLS system that combines a Mach-Zehnder type low-coherence interferometer with a microscopic optical system and a liquid immersion probe. The detection sensitivity of scattered light improved 1000 times or more compared to the conventional method, and the measurable particle diameter increased. It was possible to extend the range from several nm to several μm , which makes it possible to cover the practical particle size range. The particle size distribution quantified by this method was consistent with the TEM result, regardless of monodispersity and polydispersity. In order to discriminate the diffusion mode of the densely dispersed particle system, we developed an angle variable LC-DLS and showed that the diffusion coefficient of a PS suspension is based on translational diffusion.

It is difficult to ascertain to what extent the micro viscosity has fluctuated when the macroscopic viscosity of the dispersion system fluctuates in a concentrated system. It is necessary to deepen the basic research of the dispersion system to clarify the relationship between particles motion and micro viscosity. In the analysis, a system that can be quantified on the assumption that the viscosity is different for each particle type and particle size is required. In addition, the expression (43) is called ill-problem. It is known that it is hard to obtain a solution uniquely in the system shown in Fig.26. A method for accurately calculating the true particle size distribution is necessary, even in the polydisperse state of the system. In order to improve the usefulness of measurements, it is essential to increase the amount of measurement information by such a method as the variable angle system described in this paper.

VI Particle distribution of concentrated polydisperse suspension through high sensitivity low-coherence dynamic light scattering

In this study, I developed a low-coherence dynamic light scattering system using a high sensitivity Mach–Zehnder interferometer, which can quantify the distribution of a wide range of particle sizes in dense polydisperse suspensions. The proposed system easily quantified the dispersity of a standard mixture of particles with diameters 23 and 120 nm. I also used the proposed system to quantify changes to the dispersity of a nano-ink solution due to dilution and precipitation over time. These results indicate that the dispersity measurements of nanoparticle solutions should be performed on undiluted and fresh samples of the test solution.

1. Method

1) System

The experimental setup of the LC-DLS is based on a Mach–Zehnder interferometer (Fig. 33). The light source is a super-luminescent diode (S830-G-I-20, Superlum Co.) with a central wavelength and a spectral width of 833.6 and 16.2 nm, respectively. The low-coherence light is divided into two beams using an optical coupler with a coupling ratio of 1:99. The reference beam passes through an electro-optical modulator (EOM, EO-PM-NR-C1, Thorlabs Co.). The other beam irradiates the sample suspension and is guided by a circulator, a collimator, and a lens. Then lights scattered by the particles is collected by an objective lens and collimated into the output fiber. The two beams are mixed with a coupling ratio of 1:1, interfered with each other by the other coupler and then measured by an auto-balanced optical receiver (Model 2007, NewFocus Co.).

The single-mode fiber probe system is shown in Fig. 30. The head of the probe is placed directly in the container of a sample suspension. The container holds 10 μL of liquid. The test beam passes through the optical fiber and irradiates particles in the sample directly. Then light back-scattered from Brownian-moving particles returns to the probe. Constant temperature is maintained by the Peltier device.

I set the modulation frequency of the EOM in consideration of the bandwidth of the scattered light. We also adjusted the path length of the reference beam to match the path length of light beams scattered by particles in the suspension. The power spectrum and the temporal autocorrelation function are calculated by a PC.

The power spectrum of the detected signal had several peaks, as shown in Fig 34. One peak was located around 0 Hz. This frequency is related to both the homodyne and heterodyne spectra of the scattered light and was therefore influenced by multiple scattering events. Other peaks, located around the modulation frequency (8 kHz in this case) or its harmonics, contained only the heterodyne spectrum. The heterodyne spectrum is composed of the scattered light with path length almost equal to the path length of the reference light. By measuring the heterodyne spectrum of scattered light, with path length shorter than the mean free path length, DLS measurements can estimate the particle-size distribution even for very dense solutions.

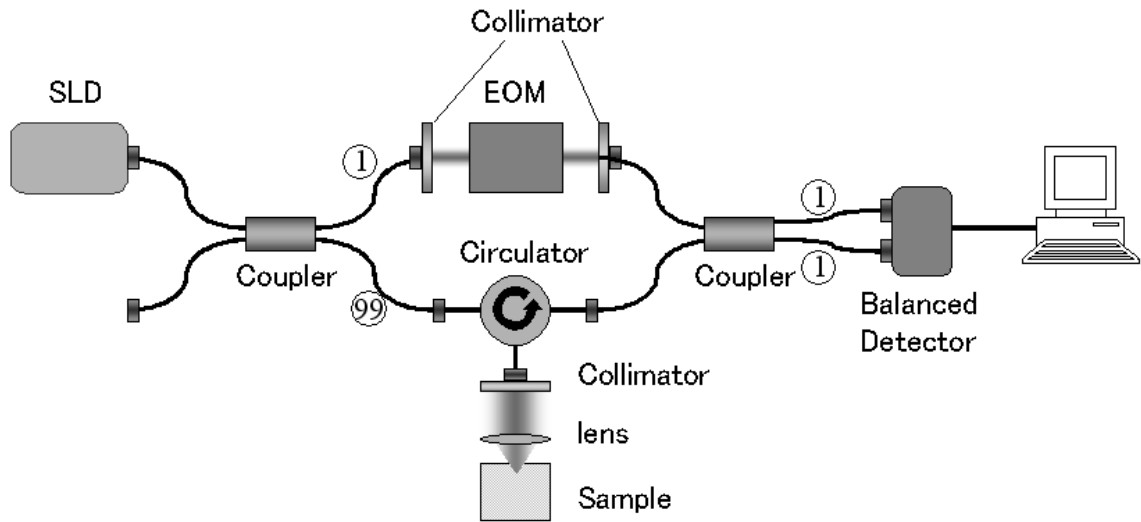


Fig. 33 A schematic of the high sensitivity, low-coherence DLS system.

2) TEM

So that I could compare the DLS measurements with results from a standard analysis method, the shapes of the standard particles were observed by transmission electron microscope (TEM JEOL JEM-1010). The particle-size distribution was then calculated after binarization using particle-size analysis software (Carl Zeiss KS400).

3) sample

The standard suspension of 10% mass concentration polystyrene with diameters of 99, 59,

23, and 12 nm were manufactured by Okenshoji Corporation (Japan). Several mixed suspensions were also prepared. Temperature was maintained at 25 °C during measurements by a Peltier element attached to the sample stage and in contact with the measurement cell.

I also tested the proposed system with measurements of a custom prepared model nano-ink solution with 15 wt% yellow pigment using bead-mill dispersion with several additives and dispersing materials. To investigate the stability of this prepared dispersion, the fresh product was measured and then it was left at room temperature for 1 month and was then collected and measured again. Dilution operations for these measurements were performed with pure water.

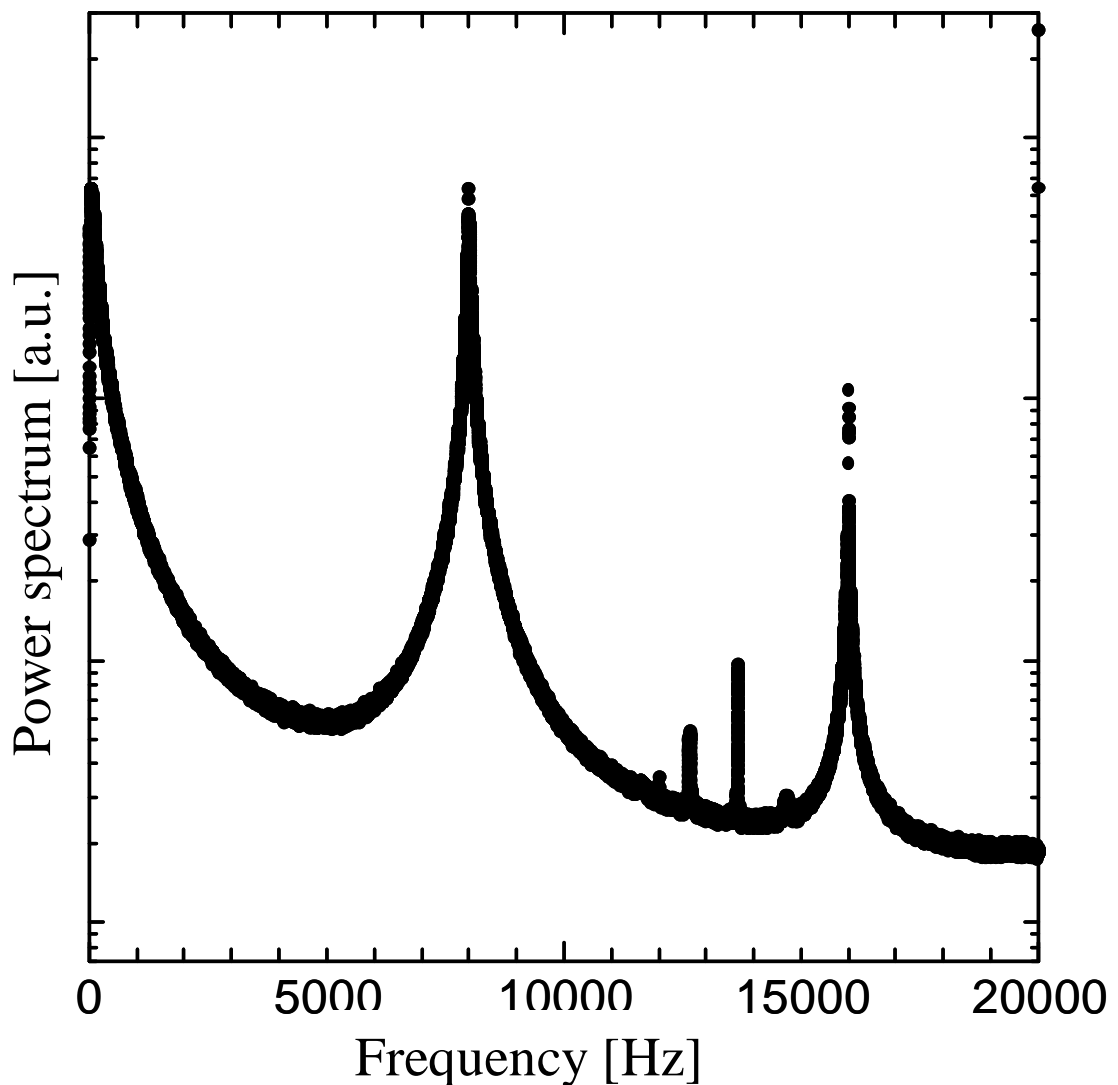


Fig. 34 An example of power spectrum measured by the high sensitivity, low-coherence DLS system.

2. Result

These tests confirmed that the proposed system can determine the particle-size distribution via the power spectrum the signal from a 10 wt% suspension of polystyrene particles with diameters of 99 and 23 nm (Fig. 35). The particle-size distributions determined using the CONTIN function are consistent with the TEM results shown in Fig. 36.

Fig. 37 shows an evaluation of the particle-size distribution for a suspension in which 10% volume concentration of polystyrene and latex particles with diameters 13 and 59 nm were mixed one-by-one. The measured particle-size distribution confirms that the two sizes of particles are mixed, although slight deviation is evident in the center particle-size. This result is sufficiently accurate as compared with the measurement result by the conventional dispersity method

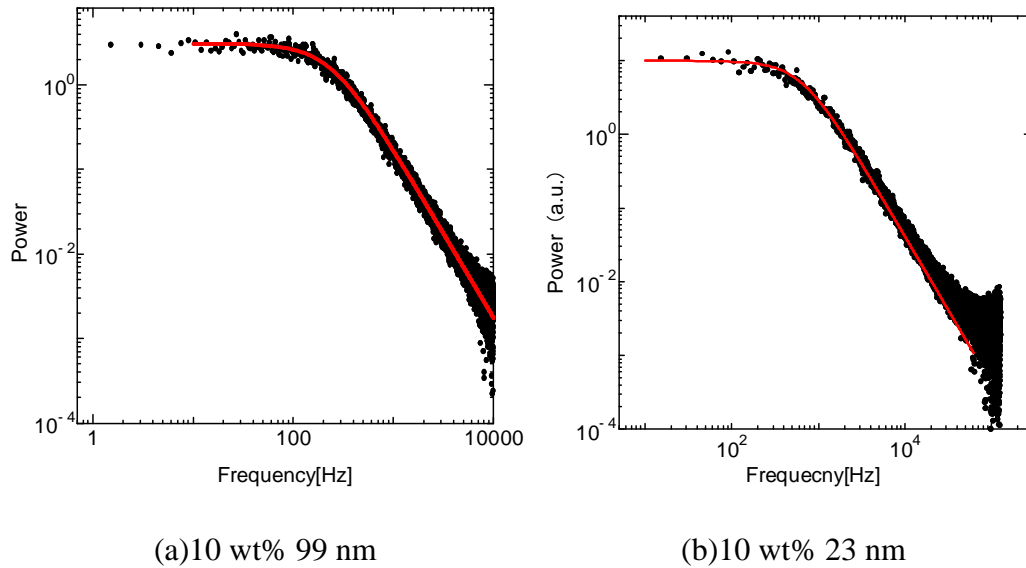


Fig. 35 Heterodyne spectrum of the scattered light from a 10 vol.% polystyrene suspension with an average particle measured by the developed LC-DLS system.

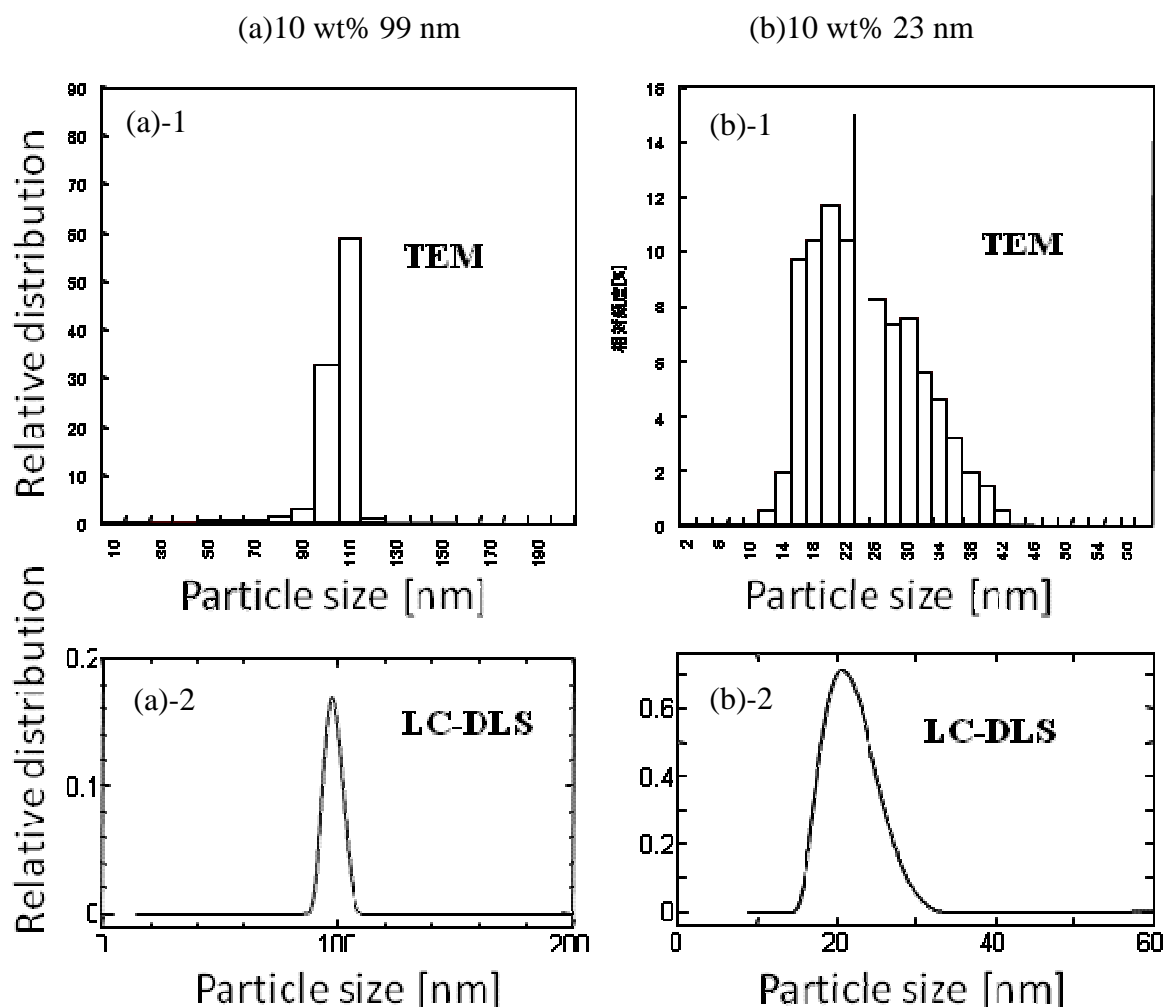


Fig. 36 Particle-size distribution estimates for a 10 vol.% polystyrene suspension. (a)-1 The histogram produced by TEM images with an average particle diameter of 99 nm. (a)-2 The size distribution of the same particle suspension with (a)-1 obtained by LC-DLS with a CONTIN method. (b)-1 The histogram of an average particle diameter of 23 nm by TEM. (b)-2 The size distribution of (b)-1 by LC-DLS with CONTIN.

Measurements of the actual pigment dispersion appear in Fig. 38 and 39. In the actual pigment dispersion, the pigment particles of about 10 nm are monodisperse. The dispersity is also affected by environmental factors such as pH and additives and processes such as aging and temperature history. Pigment particles then often collect into aggregates, resulting in a polydisperse state. Fig. 38 shows results for the particle-size distribution of the nanopigment inks. These plots indicate thixotropy and sedimentation in the nano-ink preparation. The histogram method was used for particle-size distribution analysis. Fig. 38(a) shows the results of measurements taken immediately after the particles were dispersed. Four peaks can

be observed around particle diameters of 30, 100, 500, and 5000 nm. The leftmost peak, around 30 nm, corresponds to the pigment particles and the other peaks indicate aggregates of these particles. Fig. 38(b) shows the particle-size distribution of the same sample after 1 month of storage at room temperature. The peaks at 30 and 5000 nm disappear. Particles smaller than 100 nm have aggregated into larger particles and particles of 5000 nm have precipitated out of the solution.

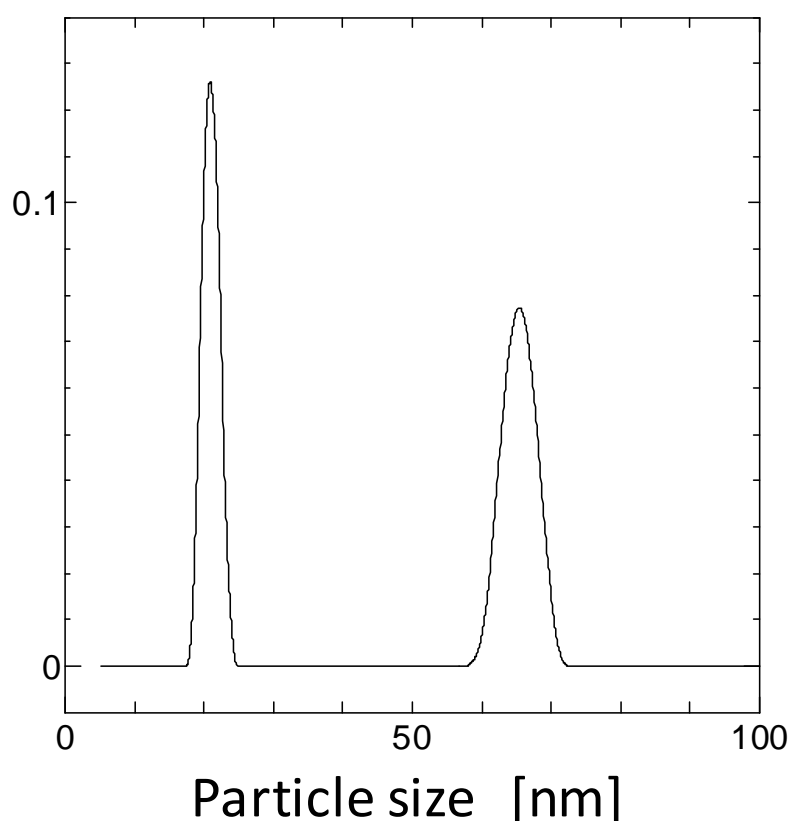


Fig. 37 The particle-size distribution estimated for a 1:1 mixture of 10 vol.% polystyrene suspensions with particles diameters of 13 and 59 nm. Distribution is acquired by CONTIN.

Fig. 39 shows the change in the dispersity of the pigment solution after dilution. The particle-size distribution is evaluated by histogram method from time-correlation functions obtained by the LC-DLS method. The particle-size distribution of the ink diluted to the weight concentrations of 0.15, 5, and 10 wt% and the undiluted solution of the 15 wt% ink are shown respectively. In the freshly prepared ink, the particle diameter is widely

distributed from 50 to 10000 nm where precipitation occurs, but as a result of dilution, large particles decrease and dispersion decreases. Since the agglutination size of the particles decreases by the dilution operation, it was found that the particles are softly flocculated due to the weak interaction among the particles because of the short distance between the particles in the concentrated dispersed particle system. This indicates that the dispersity is changed by dilution. In the conventional DLS process, dilution is necessary so that singly scattered light can be detected, but our results show that the dispersity is affected by even a single dilution. Since the dispersity of nanoparticles in solution is very unstable, this suggests that careful particle-size measurements are necessary for plant process management and basic research. Fig. 38 and 39 demonstrate the importance of measuring the dispersity of concentrated solutions.

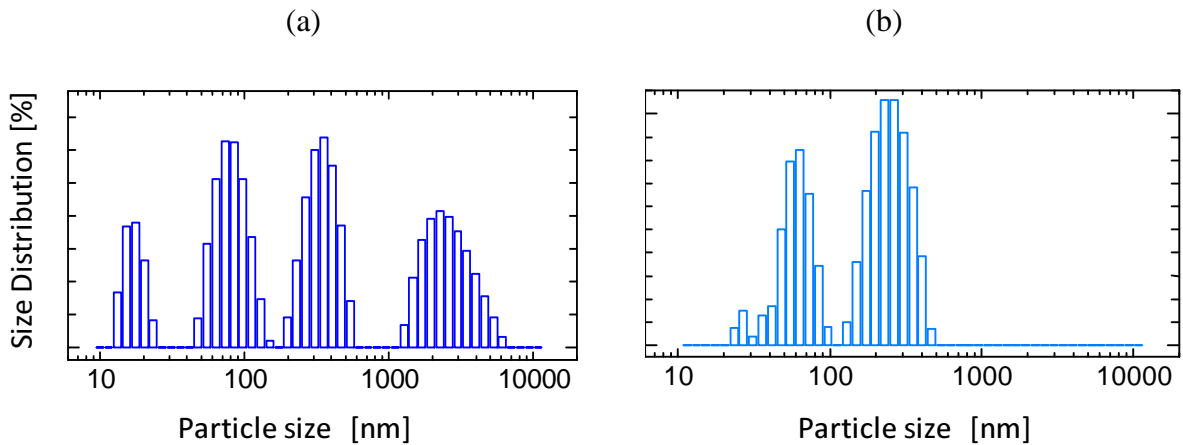


Fig.38 Change in the particle-size distribution of yellow ink over time. (a) fresh ink and (b) the same ink one month later. The distribution is obtained by a histogram method.

3. Conclusion

In this study, I showed that a high sensitivity low-coherence DLS analysis system can quantify the distribution of particle sizes ranging from several hundred nanometers to tens of nanometers in a high-concentration dispersion system. The particle-size distribution of a standard particle dispersion was compared with measurements from TEM images and these results were in agreement with each other. Measurements of a stock solution of yellow ink clarified that the particle-size distribution is affected by dilution and that the particle-size distribution in high-concentration dispersions changes with time. This result confirms that a nanoparticle dispersion system is affected by dilution, reinforcing the usefulness of my proposed system.

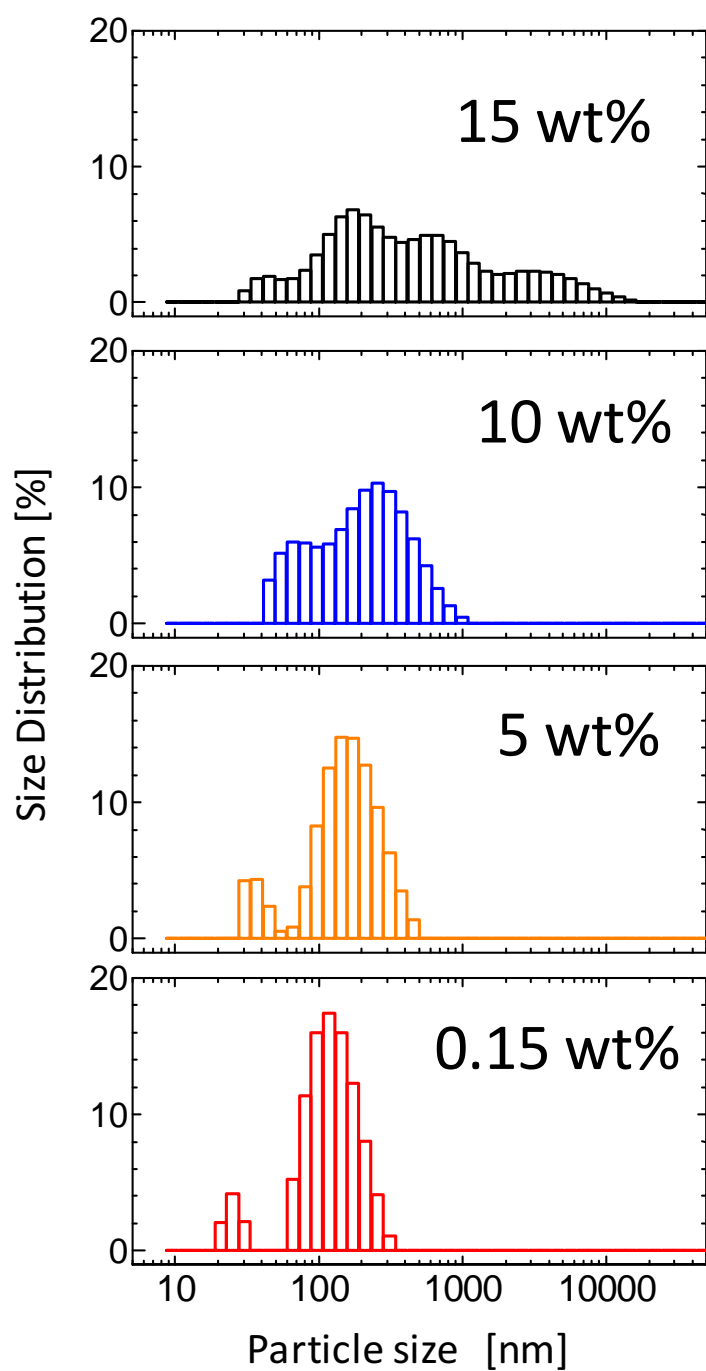


Fig.39 Change in ink particle-size distribution when diluted from 15 wt% to 0.15 wt%. The distribution is obtained by a histogram method.

VII Conclusion

One-shot ultraviolet-visible spectroscopy for application in the research and development of cosmetic products, such as skin, painted products, printed matter, thin-type displays, subjects of medical diagnosis and cosmetics, paintings and lacquer, and other cultural properties, as well as their reproduction using UV- and visible-light one-shot SD-OCT and full-color OCT, was developed. Subsequently, I carried out a color diagnosis of the skin nondestructively and clarified the internal structure of the multilayered film and the propagation characteristics of visible light. For the first time, tomographic images showing ultraviolet rays (UV-A) reaching the dermis and tomographic images of human skin using the wavelengths of the three primary colors—red, green and blue—of visible light were acquired. We also developed a full-color OCT and applied our method to a model using white/yellow samples. Further, I developed a method to achieve real-color compensation of the lower layer of human skin, which is altered by the influence of the upper layer, and applied our method to human skin. The dermis in the cheek was yellower and darker than the skin on the inner back arm was shown.

In the suspensions of ink, nanocomposite material, cosmetics, liquid preparations, etc., measurement is performed without destroying the state of the concentrated dispersion, so that a highly sensitive, low coherence dynamic light scattering device and I developed a dipping probe and a variable angle system using SM-fiber probes. This makes it possible to non-destructively quantify a wide range of dispersed states, from a single nanometer to micrometer size. Moreover, by using nanoparticles, it is possible to carry out measurement covering an industrially important particle size range. It became so. In the state of actual liquid, clarified structure of ink and diffusion type of particle were clarified.

In the future, by collectively using fundamental technologies such as miniaturization, high resolution, and improved color reproduction accuracy, I believe it will be an important foundational technology for industry, medical care and culture. Characteristic understanding of light propagation behavior in living bodies is also only an initial stage. Furthermore, by combining AI, 3D vision, and other technologies, new applications, services and inspection methods can be developed. Hence, I expect further progress in this field.

VIII References

- [1] A. Munakata, et al., Proceedings of The Japan Society of Color Sciences Cosmetics and Skin and Face Study Group, 1, 1-32 (2014).
- [2] W. Manuskiatti, D. Schwindt, and H. Maibach, "Influence of Age, anatomic site and race on skin roughness and scaliness," *Dermatology*, 196(4), 401-407 (1998).
- [3] K. Suh, H. Roh, S. Choi, Y. Joen, K. Doh, J. Bae, and S. Kim, "A long-term evaluation of erythema and pigmentation induced by ultraviolet radiations of different wavelengths," *Skin Res. and Technol.*, 13(4), 360-368 (2007).
- [4] A. Besaratinia, "Wavelength dependence of ultraviolet radiation-induced DNA damage as determined by laser irradiation suggests the cyclobutane pyrimidine dimers are the principal DNA lesions produced by terrestrial sunlight," *FASEB J.* 25(9), 3079-3091 (2011).
- [5] T. R nger, "How different wavelengths of the ultraviolet spectrum contribute to skin carcinogenesis: The role of cellular damage responses," *J. of Invest. Dermatology*, 127(9), 2103-2105 (2007).
- [6] L. Rittie, G. Fisher, "UV-light-induced signal cascades and skin aging," *Ageing Research Reviews*, 1(4), 705-720 (2002).
- [7] Maeda, N. Arakawa, M. Takahashi, and Y. Aizu, "Monte Carlo simulation of spectral reflectance using a multi layer skin tissue model," *Opt. Rev.* 17(3), 223-229 (2010)
- [8] W. A. G. Bruls, et al., "Transmission of human epidermis and stratum corneum as a function of thickness in the ultraviolet and visible wavelengths," *Photochem. Photobiol.* 40(4), 485-494 (1984).
- [9] Mark E. Brezinski MD, *OPTICAL COHERENCE TOMOGRAPHY* (ACADEMIC PRESS, 2006).
- [10] E. Li, et. al., "Three-dementional multi-contrast imaging in vivo human skin by Jones matrix optical coherence tomography," *Biomed. Opt. Express*, 8(3), 1290-1305 (2017).
- [11] S. Huang, et. al., "in-vivo imaging of retinal hemodyanamics with OCT angiography and Doppler OCT," *Biomed. Opt. Express*, 7(2), 636-676 (2016).
- [12] A. Dubois, et. la., "Ultrahigh-resolution full-field optical coherence tomography, " *Applied Optics*, 43(14), 2874-2883 (2004).
- [13] Dalimier, et al., "High resolution in-vivo imaging of skin with full field optical coherence tomography," *Proc. SPIE* 8926, 89260P (2014).
- [14] J. B. Eom, E. J. Min, and B. H. Lee, "Visible and near infrared wavelength photonic

- crystal fiber splitter for multiwavelength spectral domain optical coherence tomography,” *Proc. SPIE* 8264, 82641F (2012).
- [15] B. Povazay, et al., “Submicrometer axial resolution optical coherence tomography,” *Opt. Lett.* 27, 1800-1802 (2002).
- [16] F. Robles, C. Wilson, G. Grant and A. Wax, “Molecular imaging true-colour spectroscopic optical coherence tomography,” *Nature Photonics*. 5, 744-747 (2011)
- [17] F. Robles, R. N. Graf, and A. Wax, “Dual window method for processing spectroscopic optical coherence tomography signals with simultaneously high spectral and temporal resolution,” *Opt. Express* 17(8), 6799–6812 (2009).
- [18] V. Jaedicke, S. Agcaer, F. Robles, D. Jones, S. Goebel, N. Gerhardt, H. Welp, and M. Hofmann, “Comparison of different metrics for analysis and visualization in spectroscopic optical coherence tomography,” *Biomed. Opt. Express* 4(12), 2945 (2013).
- [19] S. Chen, Q. Liu, X. Shu, B. Soetilno, S. Tong, and H. Zhang, “Imaging hemodynamic response after ischemic stroke in mouse cortex using visible-light optical coherence tomography,” *Biomed. Opt. Express*, 7(9), 3337 (2016).
- [20] S. Leelajariyakul, H. Noguchi, S. Kiatkamjornwong, *Progress in Organic Coatings*, 62 , 145–161 (2008).
- [21] A. Haroun, H. Diab, O. Hakeim, *Carbohydrate Polymers*, 146, 102–108 (2016).
- [22] J. Carbajo, A. Tolosana-Morachel, J. Casas, M. Farados, A. Bahamonde, *Applied Catalysis B: Environmental*, 221, 1–8 (2018).
- [23] C. Petchthanasombat, T. Tiensing, P. Sunintaboon, *J. Colloid. And Interf. Sci.*, 369, 52–57 (2012).
- [24] Bruce J. Berne, *Dynamic Light Scattering: With Application to Chemistry, Biology, and Physics*, 1st ed. (Krieger Pub Co, 1990).
- [25] K. Bizheva, A. Siegel, D. Boas, *Phys. Rev. E*, 58, 7664 (1998).
- [26] A. Wax, C. Yang, R. Dasari, M. Feld, *Appl. Opt.*, 40, 4222–4227 (2001).
- [27] A. Petoukhova, W. Steenbergen, T. Leeuwen, F. Mul, *Appl. Phys. Lett.*, 81, 595–597 (2002).
- [28] K. Ishii, R. Yoshida, T. Iwai, *Opt. Lett.*, 30, 555–557 (2005).
- [29] B. Varghese, V. Rajan, T. Leeuwen, W. Steenbergen, *J. Biomed. Opt.*, 12, 024020 (2007).
- [30] H. Xia, C. Miao, J. Cheng, S. Tao, R. Pang, X. Wu, *Appl. Opt.*, 51, 3263 (2012).
- [31] H. Xia, R. Pang, R. Zhang, C. Miao, X. Wu, X. Hou, C. Zhong: *J. Colloid. and Interf.*

- Sci., 376, 322 (2012).
- [32] T. Watarai, T. Iwai, Appl. Phys. Express, 7, 032502 (2014)
 - [33] T. Watarai, T. Iwai, Opt. Rev., 21, 378 (2014).
 - [34] W. Chenog, S. Prahl, and A. Welch, IEEE. J. Quantum Electron, 26, 2166-2185 (1990).
 - [35] M. Imada: “*Toukei-butsurigaku*” (written in Japanese), 1st ed. (Maruzen Co, 2004).
 - [36] R. Abbe: “*Toukei-rikigaku*” (written in Japanese), 2nd ed. (Tokyo Univ. Pub., 1992).
 - [37] N. A. Nassif, et al., “*In vivo* high-resolution video-rate spectral-domain optical coherence tomography of the human retina and optic nerve,” Opt. Express 12, 367-376 (2004).
 - [38] G. Hausler and M. W. Lindner, “‘Coherence radar’ and ‘spectral radar’—new tools for dermatological diagnosis,” J. Biomed. Opt. 3(1), 21-31 (1998).
 - [39] R. A. Hogg and P. Andersen “Quantum-dot diodes provide sources for optical coherence tomography,” SPIE Newsroom, April 1, 2006.
 - [40] Lister et al., “Optical properties of human skin,” J. Biomed. Opt. 17(9), 090901 (1998).
 - [41] Bashkatov et al., “Optical properties of human skin, subcutaneous and mucous tissues in the wavelength range from 400 to 2000 nm,” J. Phys. D: Appl. Phys. 38, 2543 (2005).
 - [42] Y. Matsumura and H. N. Ananthaswamy, “Toxic effects of ultraviolet radiation on the skin,” Toxicol. Appl. Pharmacol. 195(3), 298-308 (2004).
 - [43] M. Meinhard et al., “Wavelength-dependent penetration depths of ultraviolet radiation in human skin,” J. Biomed. Opt. 13(4), 044030 (2008).
 - [44] F. H. Mustafa et al., “Comparison of wavelength-dependent penetration depths of lasers in different types of skin in photodynamic therapy,” Indian. J. Phys. 87(3), 203-209 (2012)
 - [45] S. Nakamura, and H. Hirayama, “Development of one shot visible spectral domain OCT,” The 61st JSAP Spring Meeting, 17a-E6-2 (2014).
 - [46] S. Nakamura, and H. Hirayama, “Spectroscopic tomographic images of human skin,” OYO BUTURI, 84(4), 326-330 (2014).
 - [47] H. Hirayama, and S. Nakamura, “Development of ultraviolet- and visible-light one-shot spectral domain optical coherence tomography and in situ measurements of human skin,” J of Biomed. Opt., 20(7), 076014 (2015).
 - [48] W. A. Thornton, “Luminosity and color-rendering capability of white light,” J. Opt. Soc. Am, 61(9), 1155-1163 (1971).
 - [49] T. Watarai, and T. Iwai: Current Pharm. Biotech.: 13, 2562-2568 (2012).

- [50] K. Ishii, and T. Iwai: Jpn. J. Appl. Phys. 47, 8397-8401 (2008).
- [51] M. Shibayama, T. Sato, T. Iwai, and Y. Kimura: “*Hikarisanran no kiso to oyo*” (written in Japanese), 1st ed. (Kodansya Scientific Co, 2014)
- [52] S. W. Provencher: Comp. Phys. Comm., 27, 213 (1982)
- [53] S. Nakamura, Y. Sato, and K. Ishii: “High-sensitivity low-coherence dynamic light scattering and particle sizing for nanoparticles (II): “SM-fiber probe system applied to dense particle suspension,” Proc. SPIE 9232(2014), *International Conference on Optical Particle Characterization, 923201-05 (OPC 2014)*.
- [54] R. Cush, P. Russo, and H. Ricks: Macromolecules 30, 4920 (1997).
- [55] M. Shibayama, T. Norisuye, and S. Nomura: Macromolecules 29, 8746 (1996).

IX Publications

1. Spectroscopic tomographic images of human skin
S. Nakamura, H. Hirayama
OYO-BUTURI 84(4), 326-330 (2015)
2. Development of UV and visible region one-shot SD-OCT and *in-situ* measurements of human skin
H. Hirayama, S. Nakamura
J. Biomed. Opt. 20(7), 076014 (2015)
3. Development of Base Makeup Series “ASTALIFT Lighting Perfection”
M. Kinai, T. Tateishi, K. Nakamura, T. Yanagi, I. Ogaru, N. Ohira, N. Yoshida, S. Nakamura, E. Ikeda, Y. Takeda
FUJIFILM RESEARCH & DEVELOPMENT, 60, 44-49 (2015)
4. Development of Multi-Scale Optical Simulation Technique and its Application to the Analysis of “ASTALIFT JERRY AQUARYSTA”
Y. Yamagushi, N. Yoshida, H. Ishibashi, T. Tani, S. Nakamura, E. Ikeda, I. Ohgaru, T. Thiele, J. Mori
FUJIFILM RESEARCH & DEVELOPMENT, 61, 7-11 (2016)
5. Size evaluation of high-concentration dispersion particle size system: low coherence dynamic light scattering method
K. Ishii, S. Nakamura
FUNDEMENTALS AND APPLICATIONS OF LIGHT SCATTERING (Kosansha Ltd, 2014, language written with *Japanese*), 248-261
6. Development of full-color OCT and *in situ* measurements of human skin
S. Nakamura, H. Hirayama, I. Ohgaru
in preparation.

7. Particle-size distribution of concentrated polydisperse suspension through high sensitivity low-coherence dynamic light scattering
S. Nakamura, Y. Sato, K. Ishii
in preparation.
8. Development of high-sensitivity low-coherence dynamic light scattering and determinations of particle size distribution and diffusion motion modes applied to dense particle suspensions
S. Nakamura, Y. Sato, K. Ishii
in preparation.

X Conference Presentaion

1. High sensitivity of low coherence dynamic light scattering method
S. Nakamura, Y. Sato, K. Ishii
OSJ Symposium, Proceedings of OPJ 2011, Light Design Award Winner Commemorative Lecture (invited)
2. High-sensitivity low-coherence dynamic light scattering and particle sizing for nanoparticles (II):SM-Fiber probe system applied to dense particle suspensions
S. Nakamura, Y. Sato, K. Ishii
Internaional Conference on Optical Particle Characterization (POC2014), Proc of SPIE 9232, OPC 2014, 92320I (2014)
3. Development of Ultraviolet- and visible-light spectral domain optical coherence tomography and in situ measurements of human skin
S. Nakamura, H. Hirayama
International Workshop on Smart Sensing Systems (IWISS) 2016, Proceedings of the invited talks 53-57 (2016) (invited)
4. Development of Full-color OCT and *in situ* measurement of human skin
S. Nakamura, H. Hirayama, I. Ohgaru
The 24th Congress of the International Commision for Optics (ICO-24), W1D-06 (2017)
5. Skin spectroscopic tomographic image - Development of one shot visible spectroscopic OCT -
S. Nakamura, H. Hirayama
The 55th Workshop of Optical Design Research Group in JAPAN: OPTICS DESIGN, 55, 16-21 (2014) (invited)
6. Cross-sectional image revealed in ultraviolet and visible light colors
S. Nakamura, H. Hirayama
The 166th Fragrance Journal Seminar in JAPAN, (2015) (invited)
7. Tomogram examined by one-shot ultraviolet - visible spectroscopic OCT

S. Nakamura, H. Hirayama

Multidimensional Technology Optical Fusion Process Study Group 5th Research
Exchange Meeting in JAPAN, (2016) (invited)

8. Size evaluation of high concentration dispersion particle size: Improvement of sensitivity
of low coherence dynamic light scattering method

S. Nakamura, Y. Sato, K. Ishii

The 24th scattering study group meeting (2012) (invited)

Appendix

Source spectrums of Visible-OCT by using color-filters are shown in Fig.40 and their corresponding FFT are shown in Fig.41.

Blue1 Blue2 Green1 Green2 Orange Red1 Red2
 450 ± 20 nm 453 ± 33 nm 550 ± 20 nm 572 ± 38 nm 595 ± 30 nm 650 ± 20 nm 698 ± 32 nm

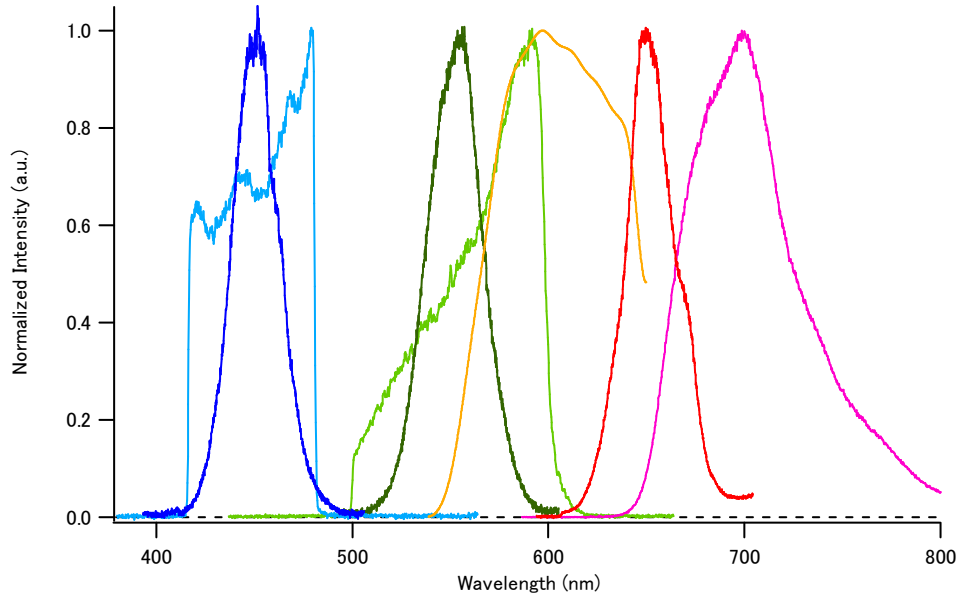


Fig.40 Source spectrums of Visible-OCT

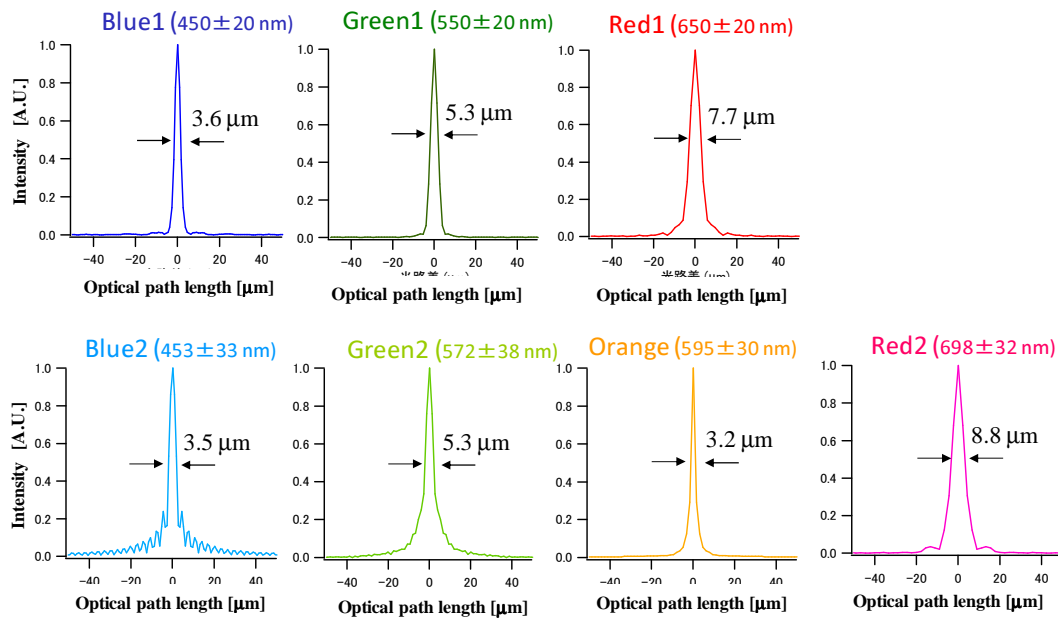


Fig.41 Source spectrum's corresponding FFT

OCT tomograms of 1951 USAF resolution target by using Red2 are shown in Fig.42. The comparison between Visible-OCT's and Near-infrared-SS-OCT's tomogram is shown in Fig.43.

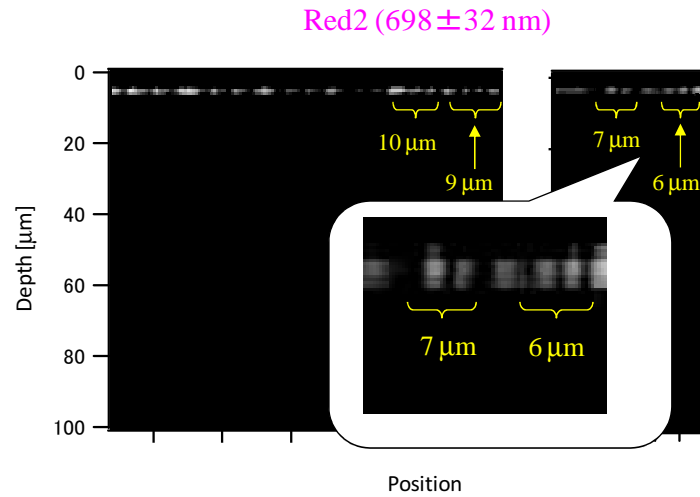


Fig.42 OCT tomograms of 1951 USAF resolution target

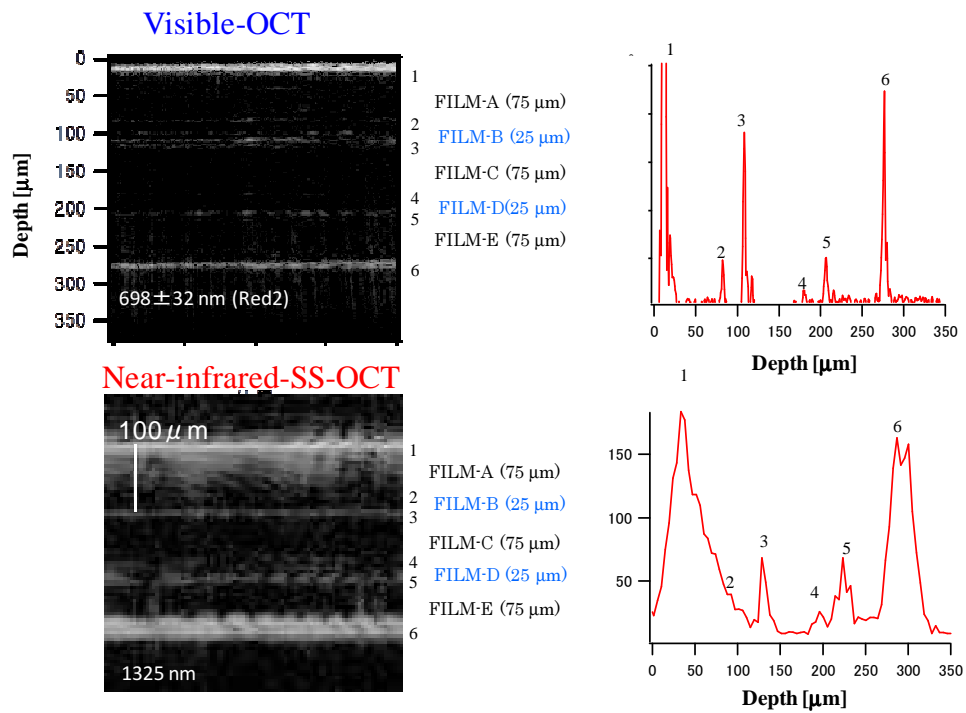


Fig.43 Comparison of Visible-OCT and Near-infrared-SS (Swept source) -OCT (a commercial product)

Acknowledgement

I am deeply grateful to Prof. Takuya Hirano who gave me the opportunity for a lecture and my doctoral thesis at Gakushuin University. It has become a good time to summarize my work. The non-destructive measurement is coincidence with the past work for a Bose-Einstein condensate during my university days.

I am also thankful to Prof. Ichiro Arakawa and Prof. Masahito Watanabe for receiving the sub-chief examiner of the paper. They have read my paper and got lots of advice.

I would like to extend my thanks to Associate Prof. Katsuhiro Ishii of the Graduated School of the Creation of the New Photonics Industries for advice on the interference measurements and LC-DLS. When I was searching for the reason why the quantification of particle dispersion did not work correctly in R & Ds, I found his series of research papers and got his consultation. It is fun to talk with and taught by him about light scattering phenomena.

Mr. Yuuki Sato had been working on the development of LC-DLS together. Although he was involved as the first job he just entered into FUJIFILM company, interpretation of polydisperse particles and technology development of LC-DLS advanced with his efforts and cooperation. Now he is devoted to inkjet research. I think he is the excellent and sincere man.

Mr. Heijiro Hirayama has proceeded with the development of the OCT together. Since it was research on a new field such as cosmetics, although there were many tough times in terms of its utilization and the date to due, we worked together late and we were able to overcome many difficulties. His dedicated effort was important to the study.

I also received support from Ms. Keiko Mesaki, Ms. Yumi Kobayashi, Ms. Sayaka Harada, Mr. Yoshiki Takazawa, Mr. Kazuaki Noto, Ms. Megumi Seki (Kasezawa) for taking care of my daily request for analysis from many departments despite having many impossible difficulties.

I also acknowledge the advice and encouragement of Ms. Ikuko Ohgaru, Dr. Shigeki Kageyama, and Mr. Masahiro Eto of Pharmaceutical & Healthcare Research Laboratories. I got advice and support to tell me the needs necessary for cosmetic development along various products and to connect between technology and product development. The idea of OCTs developed was noticed and nurtured in such a situation.

Dr. Yosuke Miyashita, Mr. Junichi Mori, Dr. Naoki Hayashi and Mr. Takafumi Noguchi of Analytical Technology Center of FUJIFILM, as direct superiors of me and as seniors to my work, I received many supports for how to proceed with my work. They supported me in various ways.

Finally I thank my familiy, Ayako, Masataka, Takaaki, Kenichiro, Yukiko, Tunemitsu, and Syoko. It took time to finish this paper. In particular, my wife made time for me, it was a difficult period of child rearing for my 2 and 3 year old sons. My parents-in-law Tsunemitsu and Syoko also took care of the children during this time. My father and mother recommended me to obtain my doctorate. I am very grateful to you.

